

X-ray observations of GX 301–2

Bachelorarbeit aus der Physik

Vorgelegt von

Nicolas Zalot

13. September 2021

Dr. Karl Remeis-Sternwarte, Bamberg
Friedrich-Alexander-Universität Erlangen-Nürnberg



Betreuer: Prof. Dr. Jörn Wilms

Abstract

In binary systems with highly magnetized neutron stars mass is transferred from the companion star onto the compact object. Near the neutron star the accreted material flows in accretion columns. The number and geometry of columns is still not confirmed for the system GX 301–2. I aim to discuss different scenarios of the accretion columns in this system. For this purpose the pulse-phase variabilities of cyclotron line parameters are analyzed in detail. I analyze an observation of the neutron star during the pre-periastron flare, where it is in its high luminosity state. The phase-averaged spectrum is fitted to three different continuum models. The best model is used in the analysis of the phase-resolved spectrum where the spectrum is analyzed in ten equally spaced phase bins. I confirm the previously found variability of the cyclotron line energy of the 35 keV line; the 50 keV line also shows significant phase-variability. From this I conclude that the lines are most likely not related and expected to form in different accretion columns; this theory is inconsistent with the model proposed by Fürst et al. (2018). I discuss possible scenarios of the accretion columns that could form the cyclotron lines.

Contents

1	Introduction	5
2	Neutron stars: theoretical background	5
2.1	Formation	6
2.2	Properties of neutron stars	7
2.2.1	Mass and radius	7
2.2.2	Rotational period	7
2.2.3	Magnetic field strength	8
2.3	Neutron star classification	8
2.4	Accretion in magnetized neutron star systems	10
2.4.1	Accretion disks	10
2.4.2	Wind accretion	10
2.4.3	Accretion near the neutron star	11
2.5	Landau quantization	13
2.6	Cyclotron Resonant Scattering Features	14
2.7	Radiation within the accretion column	17
3	Observed system and observation overview	20
3.1	The system GX 301–2	21
3.2	Cyclotron lines in previous papers	21
3.3	<i>NuSTAR</i> and its role in CRSF detection	24
3.4	Observation overview	26
4	Data processing	29
4.1	Data extraction	29
4.2	Data analysis methods	29
4.3	Fitting approach	30
4.4	Data reduction	31
4.5	Cash statistics	32
5	Spectral models	33
5.1	Continuum models	33
5.2	Emission lines	35
5.3	Absorption in the interstellar medium	35
5.4	Absorption near the source	36
5.5	Cyclotron lines	38
5.6	Other spectral components	38

6	Phase-averaged spectroscopy	39
6.1	Comparison of models	39
6.1.1	Cutoffpl model	39
6.1.2	FDcut model	41
6.1.3	NPEX model	41
6.2	Luminosity of the observation	42
6.3	Cyclotron lines in the phase-averaged spectrum	43
7	Phase-resolved spectroscopy	48
7.1	Determination of the pulse period	48
7.2	Phase bin extraction	49
7.3	Spectral analysis	49
7.4	Phase dependency of parameters	52
7.5	Impact on the phase-averaged spectrum	53
8	Discussion and comparison to previous papers	54
8.1	CRSF parameters	54
8.1.1	CRSF parameter values	54
8.1.2	Phase-dependency of CRSF parameters	55
8.2	Implications for accretion column model	56
9	Appendix	61
9.1	Phase-averaged spectral fits	61

1 Introduction

The history of neutron stars begins in the first half of the 20th century. Surprisingly, it does not start at a telescope's ocular, but rather in the minds of theoretical physicists in the 1930s. Following the discovery of the neutron by Chadwick (1932), many physicists pondered the implications of the new particle for supernova explosions. One of the first to formulate the concept of a neutron star were Baade & Zwicky (1934). They proposed a theory where neutrons are formed in large numbers during supernovae, which eventually make up an extremely dense body with the name neutron star. Theoretical physicists Oppenheimer & Volkoff (1939) calculated equilibrium conditions of stellar matter; they found that stars with sufficient mass will “contract indefinitely” once thermonuclear energy sources are exhausted. It is now known that this contraction is caused by the halt of nuclear fusion, which leads to the breakdown of the hydrostatic equilibrium.

Not long after these theoretical postulations, the first neutron star was discovered by Giacconi et al. (1962): although they did not know what they were observing at the time, they were the first to observe X-ray radiation from Scorpius X-1. In 1967, the first observation of a compact object with a pulse profile was made by Jocelyn Bell, at the time a postgraduate student of Anthony Hewish. Hewish et al. (1968) describe their observations as a “series of pulses lasting 1.337s”. Hewish went on to win the Nobel Prize in 1974 for his female student's discovery, who herself did not receive such high honors.

Today, neutron stars (NS) are classified in two categories: isolated NS and accreting NS in binary systems. Both types of NS emit pulsed electromagnetic radiation; isolated NS show pulsed radiation in the radio band (hence the name radio pulsar) which is powered by a loss of rotational energy; accreting NS emit pulsed radiation in the X-ray band which is caused by infalling matter with high kinetic energy.

More than 50 years after the discovery of pulsars the pulse profiles of accreting neutron stars are still of great interest for astrophysicists. The pulse-variability of spectra is often related to a change in viewing angle; it is therefore a highly suitable tool to analyze anisotropic processes. For example, the pulse-variability of the emitted radiation can be used to derive models for the mass attraction mechanism of neutron stars in binary systems. The analysis of the pulse-phase-variability of the spectrum of a neutron star is the main objective of this thesis.

2 Neutron stars: theoretical background

In this section I will provide an overview over the most important and relevant physical models that describe neutron stars as well as a motivation why the following analysis provides insight over their physical characteristics. The models that only together

describe neutron stars originate in many different areas of physics. For example, the formation process of neutron stars can be explained using astrophysical supernova theory, whilst theoretical and nuclear physics explain the formation on an atomic level. Lastly, quantum mechanics lays the groundwork to explain the formation of cyclotron lines in magnetic fields.

2.1 Formation

Neutron stars are compact objects which are the remnants of supernovae. Whether a neutron star or a different object is formed depends on the characteristics of the progenitor star, especially the mass and metallicity. The here given description of neutron star formation from a core-collapse supernova is a brief summary of Janka et al. (2012); for further discussion see, e.g., Sukhbold et al. (2016) and Burrows & Vartanyan (2021).

Massive stars in the mass regime of $(8 - 10)M_{\odot}$ are potential candidates for evolving into neutron stars. Near the end of their life, their inner structure is made up of concentric shells. They result from shell-burning where heavier elements up to iron are formed by fusion in the most inner shell whilst the outer shells fuse lighter elements such as silicon, oxygen, carbon and hydrogen. At this stage the gravity-counteracting pressures are thermal pressure and degenerate electron gas pressure; one says the star is in hydrostatic equilibrium. During the shell burning the mass of the inner core increases. The mass increases up to the point where the degenerate electron pressure alone can no longer balance the gravitational pressure once nuclear fusion ceases. Based on this equilibrium condition Chandrasekhar (1931) calculated the expected mass of this core as $M_{\text{core}} \approx 1.4M_{\odot}$. This mass is therefore called the Chandrasekhar limit.

The collapse increases the pressure and temperature within the core which leads to a change in the nuclear statistical equilibrium. Extreme amounts of available energy can fuel very endothermic processes such as the fusion of elements more massive than iron. The pressure exerted on atoms allows for conditions where electron capture becomes possible: in this process an atom core absorbs an electron; thus invoking a reaction where a nuclear proton is changed to a nuclear neutron via the weak nuclear force. This converts a large fraction of protons to neutron until the matter density reaches values on the order of $\rho \approx 10^{14}\text{gcm}^{-3}$ (see Janka et al., 2012). This density value is called the nuclear density as it is the matter density within nuclei. Unaffected by the halt of this process, material is still falling onto the core. Since the density of the core cannot increase further, the infalling material bounces off.

The reflected material creates a shock front which halts at a distance of roughly $\sim 100\text{km}$ from the proto-neutron star due to dampening within the iron shell. At this stage the neutron star is already formed but still surrounded by huge amounts of stellar material and the supernova explosion is stalled. The revival of the supernova is a complicated process which is essentially neutrino-driven. For a detailed explanation see, e.g., Bethe & Wilson (1985). In short, the explosion gets restarted by high energy neutrinos origi-

nating from the core, which deposit roughly 0.1 % of their energy in the outer material. Due to this neutrino heating the material gets driven further away from the neutron star as a result of a pressure gradient. This effectively creates a quasi-vacuum at a distance of 150km from the neutron star. This condition enables the stellar matter to escape the gravitation of the neutron star. The result of this process is a supernova remnant (SNR).

2.2 Properties of neutron stars

In the following the most characteristic properties of neutron stars shall be briefly introduced.

2.2.1 Mass and radius

It is often required to make assumptions about the neutron star mass and radius. A common way to do this is to assume a canonical neutron star with a mass of $M_{\text{NS}} = 1.4M_{\odot}$. The radius of this star can be estimated from the mass and the nuclear density. This yields $R = 10\text{km}$.

Especially the true mass of a neutron star can differ significantly from the here given estimate: since the point where the shell burning stops strongly depends on the structure of the star, the fusion conditions within the core and the metallicity, the mass of the core at this stage can be lower or higher. Furthermore, neutron stars in binary systems can gain mass through mass transfer with their companion star. For a recent review on neutron star masses see, e.g., Özel & Freire (2016).

2.2.2 Rotational period

Conservation of angular momentum allows to estimate the rotational period of a neutron star. Under the assumption that both the progenitor and neutron star are homogenous spheres their angular momentum takes the form $J = I\omega = 2/5MR^2\omega$. The rotation period of the neutron star can then be expressed as

$$P_{\text{NS}} = 2\pi \cdot \frac{M_{\text{NS}}}{M_{\text{star}}} \left(\frac{R_{\text{NS}}}{R_{\text{star}}} \right)^2 \cdot P_{\text{star}}. \quad (1)$$

Assuming a canonical neutron star and a progenitor star with main-sequence properties ($R_{\text{star}} = 3 \cdot 10^6\text{ km}$, $M_{\text{star}} = 10M_{\odot}$, $P_{\text{star}} = 30\text{ d}$)¹ one finds that the rotational period of

¹Mass and radius values from https://www.atnf.csiro.au/outreach/education/senior/astrophysics/stellarevolution_mainsequence.html; rotational period as in Nielsen et al. (2013).

neutron stars is on the order of $P_{\text{NS}} \approx 1$ ms. Neutron stars are therefore fast rotators. The increase of the rotational speed is mainly caused by a change of the moment of inertia: as the outer matter falls onto the neutron star the moment of inertia decreases drastically. This is the same effect as the example of the figure skater pulling his arms inwards to rotate faster which can be found in any physics textbook. A lower limit of the rotational period can be estimated by the break-up velocity: this is the velocity v at which the gravitational force at the equator of the neutron star is no longer greater than the centrifugal force; as a consequence the object would be torn apart. Starting from an equilibrium of gravitational and centrifugal force, one finds that $P \sim 0.5$ ms for a canonical neutron star. The corresponding speed on the equator of the neutron star is on the order of $\sim 0.5c$. At this velocity relativistic effects are no longer negligible. Moreover, the compactness of the neutron star also causes relativistic effects: due to the presence of the extremely dense body, spacetime is bent in accordance with general relativity.

2.2.3 Magnetic field strength

The origin of neutron star magnetic fields is subject to ongoing research (see Peng & Tong, 2007). A comparably simple explanation is the conservation of magnetic flux. However, this model cannot explain the high magnetic field strengths observed which are on the order of $\sim 10^{12}$ G. Therefore, Peng & Tong (2007) provide a more sophisticated model for the formation of the magnetic field of neutron stars: they suggest induced Pauli paramagnetization of the degenerate relativistic electron gas within the neutron star as the source. Their proposed mechanism as well as the implications of it are beyond the scope of this thesis.

The simplest model of the magnetic field of a neutron star is the dipole model. In this model the magnetic field strength is highest near the magnetic poles.

The conditions at the poles are more extreme than any laboratory on Earth could possibly create. This is one of the reasons why neutron stars are so interesting objects to observe. The strongest magnetic field ever achieved on Earth was setup by Nakamura et al. (2018): in their experiment they achieved magnetic field strengths up to 1200 T. In relation to magnetic field strengths caused by natural processes at the Earth's surface this is very strong; however, compared to neutron stars this value is about 4 magnitudes smaller as NS achieve magnetic field strengths exceeding $B = 10^{12}$ G = 10^7 T.

2.3 Neutron star classification

In the following section I will explain the common classification of neutron stars and differences between them. Neutron stars are generally divided with respect to the energy source of their pulsed emission: isolated neutron stars are fed by the decay of rotational energy; accretion-powered neutron stars are powered by the high kinetic energy of par-

ticles within the mass transferred from the companion star.

Isolated neutron stars emit pulsed radiation in the radio band. This emission is powered by a loss of rotational energy of the neutron star; it therefore spins slower over time. This torque decay is particularly interesting in relation to the rotational period of the neutron star; the relation between the two quantities is shown in Fig. 1 for known rotation-powered pulsars. From this figure it is evident that there are mainly two subgroups

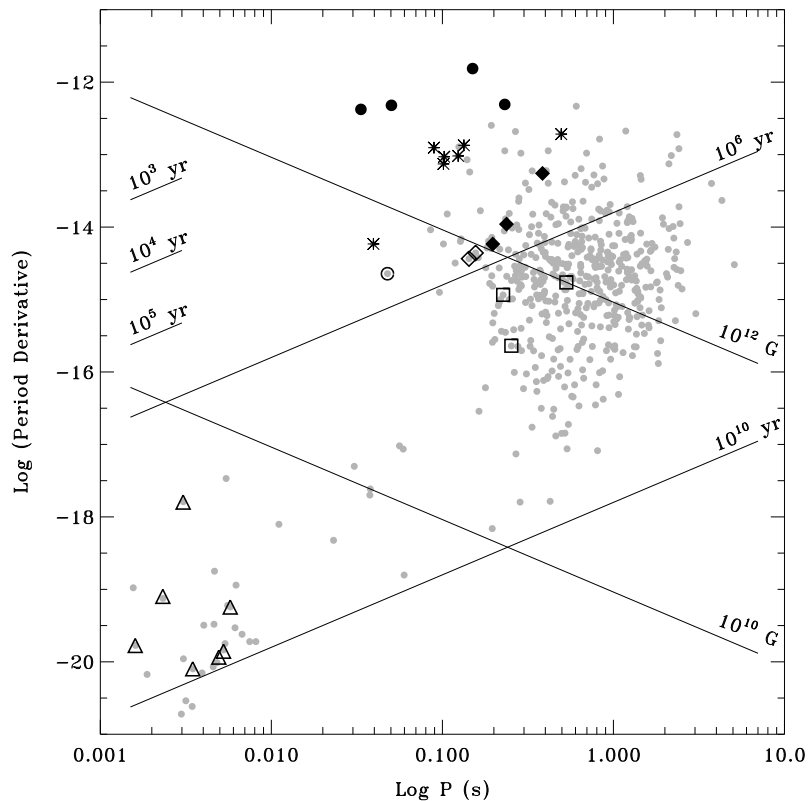


Figure 1: Diagram of P/\dot{P} of rotation-powered pulsars by Becker & Truemper (1997). Upper right corner: ordinary field pulsars; lower left corner: millisecond pulsars.

of rotation-powered pulsars: the ordinary field pulsars and the millisecond pulsars. A detailed description of isolated neutron stars can be found in van Kerkwijk & Kaplan (2007).

The second category of neutron stars are the accretion-powered neutron stars. They are in binary systems with other stars which are often called companion or donor stars as they donate matter to the compact object. This mass transfer releases large amounts of kinetic energy in form of radiation in the X-ray band.

The remainder of this thesis is devoted to accretion-powered neutron stars.

2.4 Accretion in magnetized neutron star systems

The X-ray luminosity of high mass X-ray binaries (HMXRB) neutron stars is directly caused by accretion, which is therefore a important aspect of the neutron star characterization.

Accretion in general describes the mass transfer between two bodies. In the case of X-ray binaries mass is transferred from the donor star to the compact object. This process is the energy source of their radiation: initially the accreted material has a very large gravitational potential which is successively converted to kinetic and then to radiation energy. For neutron stars, this is by far the strongest radiation source. They also emit thermal emission but at rather low fluxes in the X-ray band. It is noteworthy that the accreted material will normally be moving at supersonic speeds. The following provides a brief summary of the very detailed description of accretion mechanics by Frank et al. (2012).

The two different accretion types described in the following sections can be distinguished by the characteristics of the Roche lobe. The Roche lobe describes the volume around the donor star in which the gravitational force of the star surpasses the gravitational pull of the compact object. On its surface lies the Lagrangian point L_1 where $F_G^{\text{comp}} = F_G^{\text{NS}}$. Its name is derived from its shape, which can be thought of as a distorted sphere for binary systems. A graphical depiction of the Roche Lobe is shown in Fig. 2. During its evolution, the donor star expands. Once the stellar radius is larger than the Roche lobe material can escape through the Lagrangian point L_1 ; this material is then bound to the compact object and gets accreted by it. One can show that this transfer results in a high angular momentum of the accreted matter, which leads to the formation of an accretion disk.

A different form of accretion is wind accretion, where the compact object continuously accretes material which is emitted in a quasi-spherical geometry.

2.4.1 Accretion disks

Accretion disks form because the accreted material has angular momentum. It does not flow in a straight line towards the compact object, but forms a disk. Without a mechanism to slow down the material it would orbit the compact object. The material loses its angular momentum via viscose processes, where a fraction of its rotational energy is converted to thermal and radiative energy. This leads to a spiraling motion of the accreted material towards the neutron star. The characteristics of accretion disks can vary significantly.

2.4.2 Wind accretion

Wind accretion is based on the emission of stellar wind by the donor star in a quasi-spherical geometry. The accretion of this material by the compact object is called wind

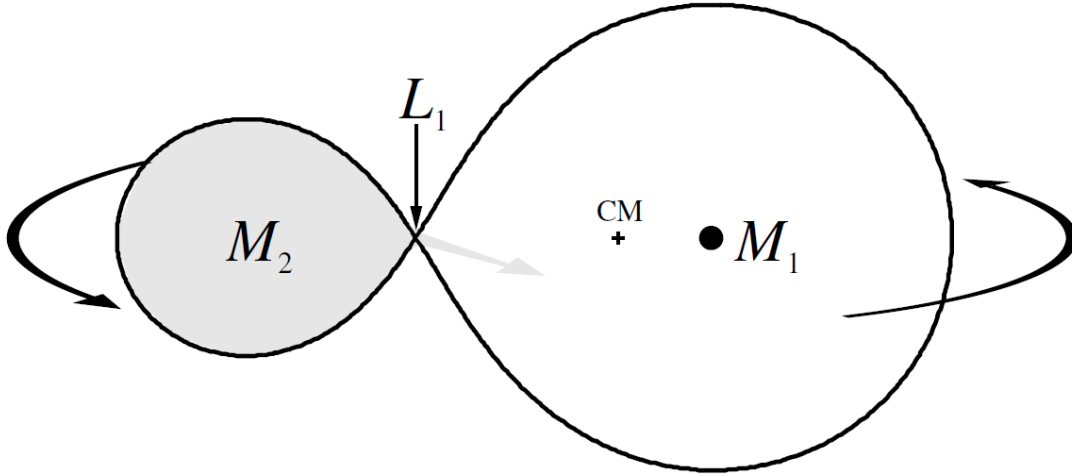


Figure 2: Illustration of Roche-Lobe Overflow by Frank et al. 2012. M_1 : neutron star (or compact object), M_2 : Donor star, L_1 : Lagrangian Point 1, CM: center of mass (Graphics not to scale).

accretion. The mass loss by the donor star can be caused by processes due to its evolution.

This accretion model was initially developed by Bondi & Hoyle (1944) who did not analyze X-ray binaries as they were not yet discovered at that time. Instead they based their analysis on stars moving through the interstellar medium. Nevertheless, their model known as Bondi-Hoyle accretion can in some cases be applied to high mass X-ray binary systems. Wind accretion can be further divided into supersonic Bondi accretion and subsonic settling accretion. A detailed description of both mechanisms can be found in Shakura et al. (2015).

2.4.3 Accretion near the neutron star

To study the behavior of accreted material near the neutron star one has to assess the conditions in this area, which are dominated by magnetic fields. The following summary follows the description by Frank et al. 2012.

The magnetic field of the neutron star can be thought to be a dipole field as a general approximation. Since for the strength of the field the proportionality $B \propto r^{-3}$ holds, the magnetic field does not influence the material at very large distances. The magnetic pressure has an even higher radial dependence, $P_{\text{mag}} \propto r^{-6}$. Far away from the neutron star the influence of the magnetic field is therefore negligible.

This changes at the point where the magnetic pressure is as strong as the ram and gas pressure. From this point onwards, the magnetic field dominates the path of the accreted material. This is due to the fact that the accreted material is highly ionized and therefore

couples to the magnetic field. The distance from the neutron star center at which the magnetic pressure equals the sum of gas and ram pressure is called the Alfvén radius. It can be roughly estimated as

$$r_M \approx 5.1 \times 10^8 \dot{M}_{16}^{-2/7} \cdot m^{-1/7} \cdot \mu_{30}^{4/7} \text{ cm} \quad (2)$$

where \dot{M}_{16} is the accretion rate in units of 10^{16} g s^{-1} , m is the mass of the accreted particle in g, μ_{30} is the magnetic moment in units of 10^{30} G cm^3 .

Since the mass accretion rate, \dot{M} , of the neutron star is closely related to the accretion-powered luminosity, one can also calculate the Alfvén radius in terms of the luminosity as

$$r_M \approx 2.9 \times 10^8 \cdot m^{1/7} \cdot R_6^{-2/7} \cdot L_{37}^{-2/7} \cdot \mu_{30}^{4/7} \text{ cm} \quad (3)$$

with R_6 as the neutron star radius in units of 10^6 cm and L_{37} as the luminosity in units of $10^{37} \text{ erg s}^{-1}$.

Within the Alfvén radius the accreted material moves along the magnetic field lines. Through this mechanism the material mainly falls onto the neutron star surface at the magnetic poles of the star and not distributed across the whole surface. The area where material falls onto the neutron star is the so-called accretion column. A graphical illustration of an accretion column is shown in Fig. 3.

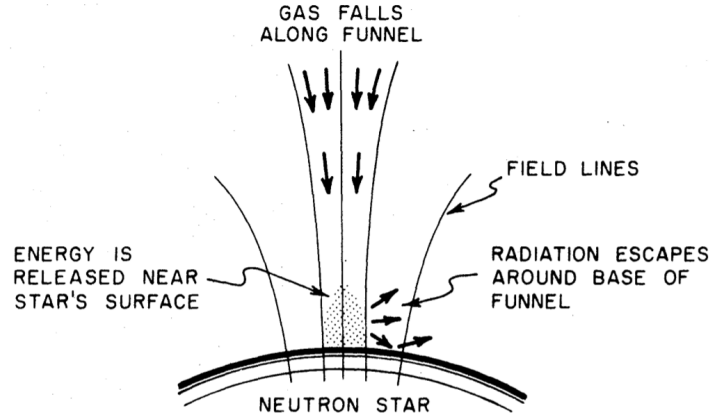


Figure 3: Illustration of the accretion column at the magnetic pole of the neutron star by Davidson & Ostriker (1973).

The accretion process described up until now is continuous and does not account for any outbursts or flares of the compact object. One possible mechanism which is responsible for luminosity increase is a change in the mass accretion rate \dot{M} . If the neutron star passes through a comparably dense region with much material the mass accretion rate and therefore the X-ray luminosity of the source increases. Some systems show periodic variations in luminosity over their orbital phase; this phenomenon can be caused

by passing through an accretion stream. For the discussion of outbursts of magnetars (neutron stars with magnetic fields exceeding 10^{13} G) see, e.g., Roberts et al. (2021) or Ajello et al. (2021).

2.5 Landau quantization

Due to the high magnetic field strength present in the vicinity of the neutron star's surface Landau quantization becomes important. It describes the quantization of the movement of electrons perpendicular to a magnetic field. It is not an effect of the electron's spin, but rather a quantum mechanical effect. It was first proposed by Lev Landau, a Soviet physicist. This short description of this effect follows Landau (1930).

The velocities of a free electron moving through a magnetic field $\vec{B} = \hat{e}_z \cdot B_z$ are given as

$$v_x = \frac{1}{m} \left(p_x - \frac{eB_z}{2c} \cdot y \right), \quad v_y = \frac{1}{m} \left(p_y + \frac{eB_z}{2c} \cdot x \right), \quad v_z = \frac{p_z}{m} = \text{const.} \quad (4)$$

One can see that these velocities describe an elliptical motion around the z -axis. It is noteworthy that the velocity along the z -axis does not depend on the magnetic field strength.

To derive the energy eigenvalues from the corresponding Hamiltonian \hat{H} one needs to solve the time-independent Schrödinger equation $\hat{H}\psi = E_n\psi$, where ψ is the wave function of the electron and E_n the n -th energy eigenvalue. As a Hamilton function the classical kinetic energies in the x - and y -dimensions are used since the movement along the z -axis does not depend on the magnetic field strength. To solve this eigenvalue problem Landau considers the commutation relation

$$[v_x, v_y] = \frac{\hbar}{i} \frac{eB_z}{cm^2} = \text{const.} \quad (5)$$

Since this relation is non-vanishing and poses similarities to the position impulse commutator $[p, q] = \hbar/i$ one introduces coordinates P and Q so that $[P, Q] = \hbar/i$. They are related to the velocities via

$$v_x = \frac{P}{\sqrt{m}}, \quad v_y = \frac{eB_z}{cm^{3/2}} Q. \quad (6)$$

Inserting this into the Hamiltonian yields

$$\hat{H} = \frac{1}{2} \left[P^2 + \left(\frac{eB_z}{mc} \right)^2 Q^2 \right]. \quad (7)$$

which corresponds to the Hamiltonian of a linear oscillator with mass m and frequency $\omega = eB_z/(mc)$. Using the known energy eigenvalues of a linear oscillator the energy eigenvalues of this system can be easily computed:

$$E_n = \left(n + \frac{1}{2}\right) \hbar\omega = \left(n + \frac{1}{2}\right) \frac{e\hbar}{mc} B_z \quad (8)$$

where $n \in \mathbb{N}$. This implies that electrons, other fermions and bosons have discrete energies perpendicular to a magnetic field. The above mentioned frequency ω is called the cyclotron frequency.

In the context of resonant scattering the energy difference between two Landau levels is of great importance. The energy difference between two adjacent Landau levels is given as

$$\Delta E = E_{n+1} - E_n = \frac{e\hbar B_z}{mc} \cdot \left(\left(n + 1\right) + \frac{1}{2} - n - \frac{1}{2} \right) = \frac{e\hbar B_z}{mc}. \quad (9)$$

This expression does not depend on the level itself, implying that Landau levels are equally spaced. Since the here used Hamiltonian only includes the classical kinetic energy terms and neglects relativistic terms this equal spacing is only valid as an approximation. Therefore, the energy difference between two adjacent levels in first order only depends on the magnetic field strength B and the mass m and charge q of the particle involved.

2.6 Cyclotron Resonant Scattering Features

Cyclotron resonant scattering features (CRSFs) are absorption features caused by resonant scattering between photons and electrons in strong magnetic fields, which already hints that they are very common in highly magnetized neutron stars.

Cyclotron lines are formed in the so-called line-forming region near the neutron star surface, where the magnetic field strength is of the order of 10^{12} Gauss. This section provides a brief summary of the detailed description of CRSF formation presented by Schwarm (2017) and Staubert et al. (2019).

The prerequisite for cyclotron line formation are charged particles within the accreted material, which falls towards the neutron star surface with supersonic speed. For highly magnetized neutron stars in binary systems mostly electrons play a key role in the formation of CRSFs; other particles will be discussed at the end of the section.

One of the earliest observations of cyclotron lines can be seen in Fig. 4: the spectrum of Her X-1 shows a negative excess in flux at an energy of approximately 45 keV.

The fundamental line energy is the energy which a photon loses through resonant scattering with an electron which transitions from Landau level n to $n + 1$. This energy is equal to the expression in equation 9. Dividing this by $1 + z$ where z accounts for the gravitational redshift of the line, one finds the general formula for the fundamental line

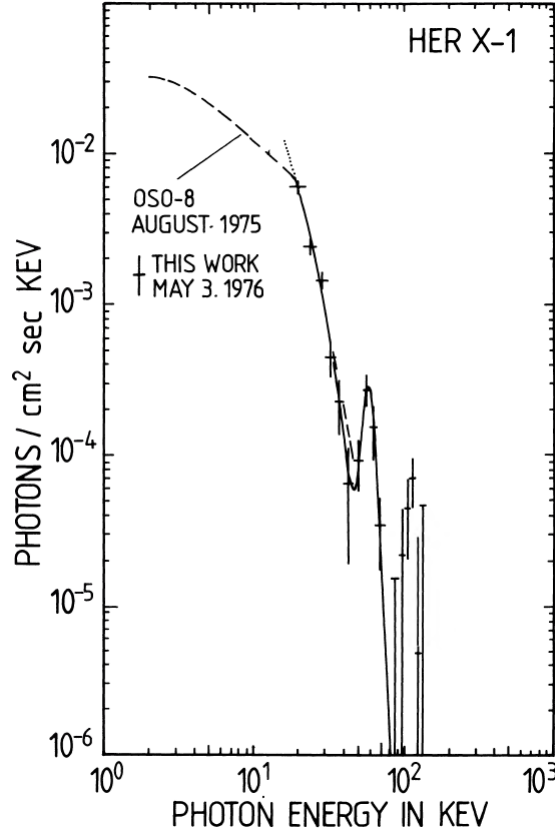


Figure 4: Cyclotron lines seen in the X-ray spectrum of Her X-1. Figure taken from Truemper et al. (1978).

energy as

$$E_{\text{cyc}} = \frac{1}{1+z} \cdot \frac{\hbar e B}{m_e c}. \quad (10)$$

To get a more intuitive understanding of this expression one can insert all physical quantities and use common astrophysical units; this yields the so-called $12B12$ rule:

$$E_{\text{cyc}} \approx \frac{n}{1+z} \cdot B_{12} \times 11.6 \text{keV}. \quad (11)$$

where B_{12} is the magnetic field strength in units of 10^{12} Gauss. The fundamental line energy can be calculated by simply evaluating this expression at $n = 1$.

The transition process of electrons between two Landau levels has similar properties as a transition in atomic physics: in the Coulomb field of the nucleus electron energies are quantised. In both cases, electrons can reach higher energy levels by resonant scattering with energized photons; they also deexcite again through scattering with photons. In the case of Landau levels, the excitation of electrons causes an absorption feature in the

spectrum at the cyclotron energy E_{cyc} . It is also possible for electrons to transition to higher Landau levels through only one scattering process. This leads to the formation of multiple cyclotron lines, whose energies are integer multiples of the fundamental line energy. These so-called harmonic lines have smaller optical depths, which often complicates their observation.

Cyclotron resonant scattering features are of great interest when assessing the characteristics of neutron stars. As their line energies are directly proportional to the magnetic field strength in the line-forming region, one can estimate the magnetic field strength from the CRSF energy.

It is at least noteworthy that not only resonant scattering with electrons can lead to the formation of cyclotron lines. Also other charged particles, e.g. protons or nuclei, of the in-falling accreted material have discrete momenta perpendicular to the magnetic field lines. Due to the fact that $E_{\text{cyc}} \propto m^{-1}$, cyclotron lines formed by protons are only observable in the X-ray band if the magnetic field strength of the neutron star compensates for the mass ratio of proton to electron. In general, the magnetic field strength should in this case be at least two magnitudes greater than the one required for the formation of electron cyclotron lines in the X-ray band.

Cyclotron lines are generally described by their line energy, optical depth, and width. It is expected that all three parameters vary significantly over the pulse phase of the neutron star due to an expected change in viewing angle. The observed width of a cyclotron line is caused by thermal broadening, which leads to the observation of photons with slightly different energies. This in turn results in broadening of emission and absorption lines.

Meszaros & Nagel (1985) derived an expression for the width of the CRSF based on the process of Doppler broadening. They find

$$\sigma_{\text{CRSF}} = E_{\text{CRSF}} \cdot \sqrt{\frac{8 \ln 2 k_B T_e}{m_e c^2}} \cdot \cos \theta \quad (12)$$

where σ_{CRSF} , E_{CRSF} are the width and energy of the cyclotron line, T_e is the electron plasma temperature and θ is the angle between the line of sight and the magnetic field axis.

From this equation it is evident that the width strongly depends on the point of view: for an observation parallel to the magnetic field where $\cos 0 = 1$ the line appears very wide; for an observation perpendicular to the magnetic field axis the line appears very narrow as $\cos 90^\circ = 0$. The here proposed limit of $\lim_{\theta \rightarrow 0} \sigma_{\text{CRSF}} = 0$ is not physically meaningful as the width can never be exactly zero. In theory the line approaches the natural line width: it stems from the energy-time uncertainty $\Delta E \Delta t \geq \hbar/2$ and is related to the natural lifetime of the electron's excited state.² Furthermore the line width has

²Information on line widths and shapes from http://www.pci.tu-bs.de/aggericke/PC4e/Kap_III/Linienbreite.htm

a lower limit that is caused by the magnetic field geometry of the neutron star. As the magnetic field is not homogeneous the angle θ cannot describe the *exact* angle between the line of sight and magnetic field axis as the angle of the magnetic field axis varies slightly due to the (assumed) dipole field of the NS. One can therefore only observe an angle of $\theta \approx 90^\circ$, which implies that there are contributions with $\theta \neq 90^\circ$ that lead to a non-vanishing width of the CRSF.

Another reason why the width of the CRSF is not zero can be found when considering the scattering cross section between electrons and photons at photon energies $E_{\text{phot.}} = n \cdot E_{\text{CRSF}}$ where $n \in \mathbb{N}$ as shown in Fig. 5. It is evident that the cross section is non-vanishing at frequencies close to the cyclotron frequency; this implies that also photons with energies slightly smaller or higher than the cyclotron energy can scatter with electrons and thusly contribute to the observed absorption feature.

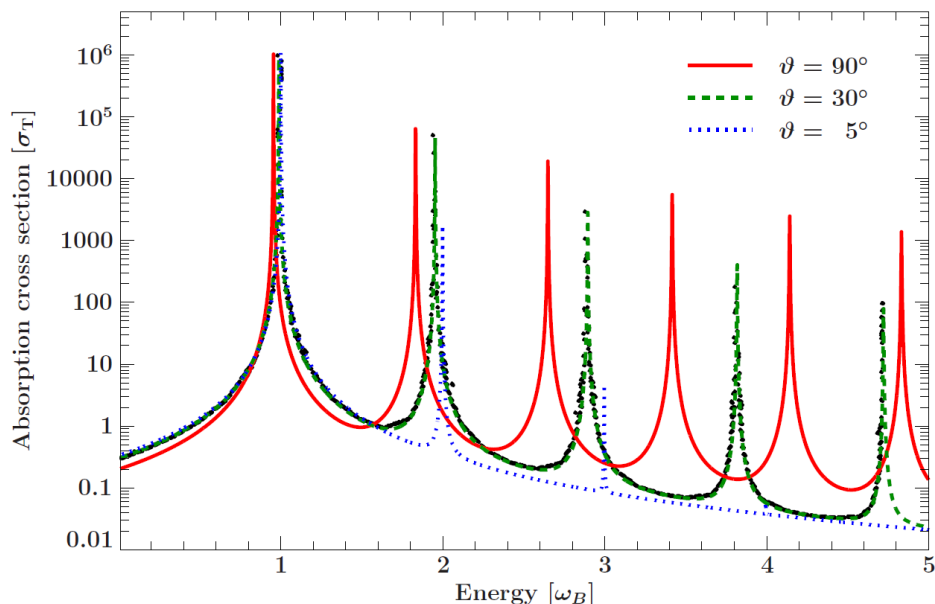


Figure 5: Cyclotron scattering cross sections for different incident angles of the photons by Schwarm (2017). The x-axis is in units of the cyclotron frequency ω_B .

2.7 Radiation within the accretion column

The accretion process leads to the radiation of large amounts of energy. For example the luminosity in the X-ray band of GX 301–2 during the 2015 *NuSTAR* observation is on the order of $L_X \approx 2.8 \cdot 10^{36} \text{ erg s}^{-1}$ (see Fürst et al., 2018). Comparing this to the solar luminosity yields $L_X \approx 730 L_\odot$. It is necessary to bear in mind that the here given luminosity of the neutron star is only from the X-ray band; the solar luminosity is given

as a bolometric luminosity.

The occurring forms of radiation shall be briefly explained in the following section, for further discussion see, e.g., Becker & Wolff (2007), Becker et al. (2012) or Sokolova-Lapa et al. (2021).

The flow of the accreted material near the neutron star surface can be described as a gas in a cylindrical geometry, which flows towards the pole in a tunnel. This theoretical tunnel through which the accreted material flows is called the accretion column. Its shell is impervious for the accreted gas but permeable for photons. The emitted radiation from this column is made up of photons that underwent Compton scattering and cyclotron interactions with infalling electrons.

There are three processes responsible for photon production: thermal blackbody radiation near the surface, cyclotron emission and Bremsstrahlung emission; where the latter is the dominant production mechanism.

Photons then interact with highly energetic particles from the accreted gas via Compton and Bremsstrahlung interaction. Furthermore, photons with high energies can interact with electrons in the magnetic field via cyclotron resonant scattering, which decreases the number of photons with energies $E_{\text{phot.}} \approx E_{\text{cyc}}$ (see Sect. 2.6). Photons can also be energized via Compton scattering.

The photon production and scattering is shown schematically in Fig. 6. As seen there, soft photons within the accretion column are energized by the super- and subsonic flow of accreted material and then emitted through the mantle of the column. The geometry of accretion columns and their dynamics is still subject to ongoing research. For example the region and height of the line-forming region for cyclotron lines is not very well understood up until now. There are many different models which come to different conclusions. One example for this is the model proposed by Poutanen et al. (2013): they suggest formation of CRSFs after the highly energetic photons are reflected from the neutron star surface. They argue that the lines cannot be formed far away from the surface as the magnetic field gradient increases with height; this would imply a non-constant magnetic field within the line-forming region which would in turn not lead to a clear absorption line.

It is expected that the observed spectrum of the accretion column changes considerably over the rotation period of the neutron star. There are multiple reasons for these pulsations: firstly, the line of sight changes and therefore the angle at which the accretion column is observed. Secondly, the magnetic and rotational axes of the neutron star are not necessarily aligned. Moreover, this implies that the part of the accretion column we see can change: it may be possible to observe both a sideward and a bird's eye view of the accretion column during the rotation period. Lastly, the strong gravitational field of the neutron star bends the path of the emitted photons. The mentioned effects can lead to changes in observed luminosity and spectral shape over the rotational period of the neutron star. A collection of pulse profiles from various pulsars can be seen in Fig. 7.

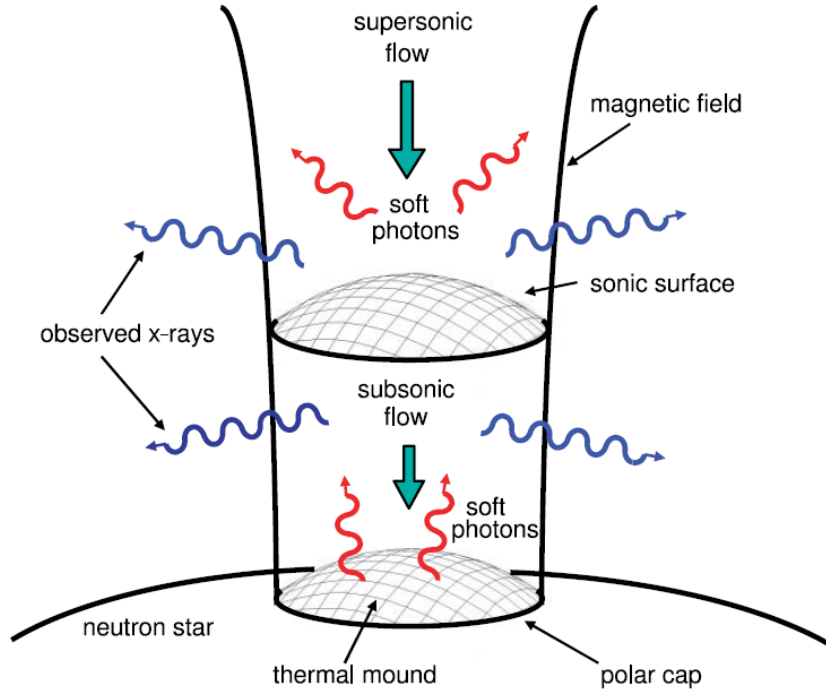


Figure 6: Radiation emitted from the accretion column. Figure taken from Becker & Wolff (2007).

It is of great interest to analyze the pulse-phase dependency of parameters that are related to the accretion column, e.g., the cyclotron centroid energies, the continuum photon index and the cutoff parameters. The analysis of the accretion column geometry of the observed system is beyond the scope of this thesis. However, the phase-dependency of relevant parameters will be discussed in detail.

Cyclotron scattering processes are of particular interest and importance for the accretion column: their energies allow to draw conclusions about their forming region. Their centroid energies can be determined from the spectrum. This energy directly depends on the magnetic field strength in the line-forming region and can therefore provide information about the height of the line-forming region. Assuming a dipole magnetic field and a canonical NS radius of $R_{\text{NS}} = 10\text{km}$ one finds height values of the order of $\sim 1\text{km}$. For example, Fürst et al. (2018) proposed a height of 1.48km for the formation of the high-energy CRSF of GX 301–2.

The existence of multiple cyclotron features poses interesting questions about the accretion column: are the lines formed in different accretion columns (e.g. at both magnetic poles) or do they stem from the same accretion column but are formed at different heights? Also, the characteristics and position of the line-forming regions are currently

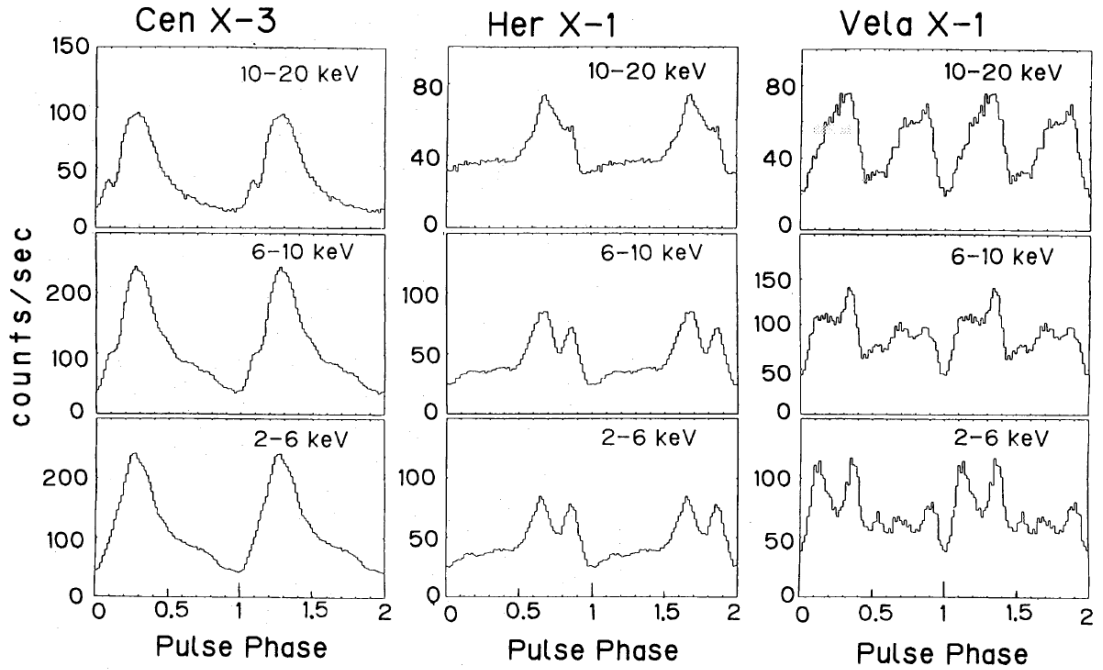


Figure 7: Average pulse profiles of three accretion-powered pulsars in different energy bands by Nagase (1989).

not well understood. It is therefore very interesting to analyze the pulse phase dependency of CRSF parameters, because the deductible dependencies can provide insight about the line-forming region which in turn can help to understand the accretion geometry.

Answering this question for the GX 301–2 system is the main objective of the observation made in late December 2020. To achieve this the phase-dependency of the cyclotron feature parameters is essential. For example, a positive correlation between their parameters suggest that they stem from the same accretion column as their parameters change similarly due to a change in observation angle.

3 Observed system and observation overview

Following the previous introduction of accreting neutron stars and the relevant concepts I will now introduce the system that will be analyzed in the proceedings of this thesis.

3.1 The system GX 301–2

The system GX 301–2 consists of two objects: a neutron star and the B type star Wray 977 (see section 1 of Kreykenbohm et al., 2004). The compact object accretes matter from its optical counterpart via stellar wind accretion (Kreykenbohm et al., 2004).

The distance between Earth and the system at hand has been subject to discussion in the past: Kaper et al. (1995) derived a distance of 5.3 kpc from its optical spectrum. Later Kaper et al. (2006) corrected their estimate to 3 – 4 kpc. Gaia measured the parallax of the source to be $p = (0.251 \pm 0.016)$ mas; the data is accessible via the Gaia EDR3 (see Gaia Collaboration et al., 2016, 2021). From this parallax the distance can be estimated to be $d \approx 4$ kpc. To derive luminosity values comparable to previous papers such as Suchy et al. (2012) and Fürst et al. (2018) a distance of $d = 3$ kpc will be used in this thesis. The distance value has far-reaching consequences for the analysis of the source: for example, using 4 kpc instead of 3 kpc would lead to systematically higher luminosities by a factor of 16/9.

To compare the orbital phases of past observations to the observation analyzed here, the orbital parameters of the neutron star orbit need to be considered. Based on observations made with *Ariel 5* and *BATSE* (see Koh et al., 1997) the orbital period is determined to be 41.5 d. The same observations also provided an estimate of the neutron star pulse period, which was determined to $P = 680$ s. Observations made in the last decades measured different pulse periods between 700 s and 675 s (see Suchy et al., 2012). For a detailed discussion of the orbital parameters see, e.g., Doroshenko et al. (2010).

A long-term light curve of the source is shown in Fig. 8. From the depicted figure it is evident that the luminosity of the source increases drastically at each periastron passage. At this point the neutron star crosses the accretion stream, which results in a short increase in mass accretion rate, which in turn leads to a higher X-ray luminosity. Shortly before the object reaches the periastron the luminosity starts to increase. For this reason this brightening is called the pre-periastron flare.

3.2 Cyclotron lines in previous papers

In the following a number of recent papers on the CRSFs of GX 301–2 will be briefly introduced and their findings regarding the CRSF variability shown. The conditions and luminosities of the here discussed observations can be seen in Table 1. The pulse-phase variability of the 35 keV cyclotron line in the different papers can be seen in Fig. 9. The whole system GX 301–2 and the orbital periods of the most recent *NuSTAR* observations are shown in Fig. 12.

Doroshenko et al. 2010 provided an estimate for the magnetic field strength of GX 301–2 based on the torque balance of the system. They found a value of $B \sim 10^{14}$ G, which is

³Doroshenko 2008 orbital parameters: <https://pos.sissa.it/067/115/pdf>

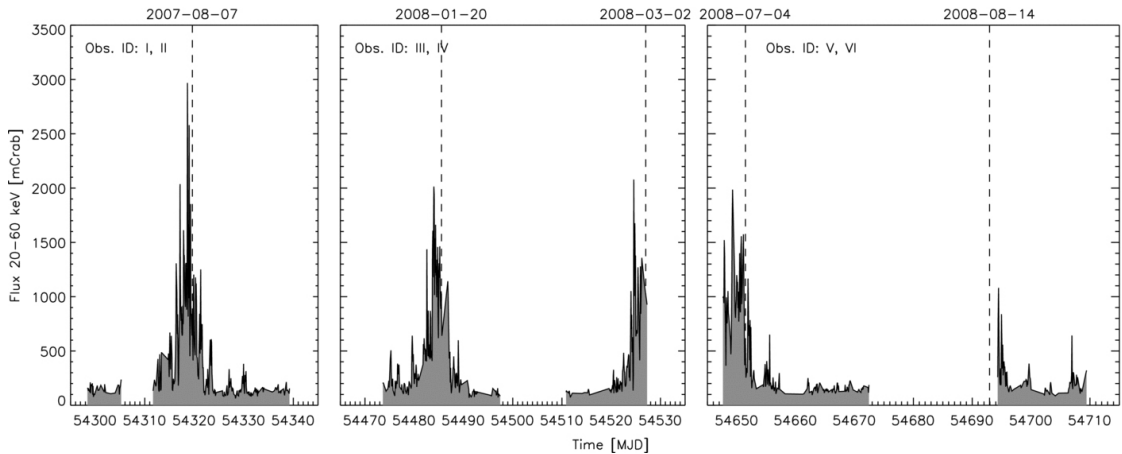


Figure 8: Light curve of long-term observation of GX 301–2 observed by *SuperAGILE* in 2007/2008, analyzed by Evangelista et al. 2010. Dashed lines show periastron passages as calculated from orbital periods given by Doroshenko at the *INTEGRAL* workshop, 2008³.

in contradiction to their value derived from the CRSF energy of $B \sim 4 \cdot 10^{12}$ G. They attempt to explain this difference by assuming that the line-forming region is at an altitude of $2.5 - 3R_{\text{NS}}$ above the neutron star surface. A value for the magnetic field strength derived by Kreykenbohm et al. 2004 from the CRSF line energy is in good agreement with the previously mentioned value. These authors studied *RXTE* observations of the neutron star made in 2001. They found that the cyclotron line shows a large variability over the pulse phase; the variation in line energy was found to be between 30 – 38 keV. They give multiple possible mechanisms for this variability: firstly, a change in altitude of the line-forming region of $\Delta h \approx 5$ km. They argue that this is rather unlikely as accretion columns have typical heights $h < 1$ km. Secondly, the variability could stem from a wide polar cap; they also disregard this mechanism as a wide polar cap would contradict the observed pulse shape, which would then be much broader. Thirdly, the radiation could be emitted from an accretion mound. They further argue that a slight CRSF variability could be caused by a change of viewing angle.

Suchy et al. 2012 analyzed two observations by *Suzaku* at different orbital phases after periastron passage. They also find a strong pulse-phase dependency of the cyclotron line parameters where the line energy varies between 30 – 40 keV. They explain this variation with a change of observed magnetic field over the pulse phase assuming a dipole model for the NS magnetic field.

The paper by Fürst et al. (2018)⁴ is of great interest for this work as they also analyze observations made with *NuSTAR*, which is the telescope also used in this thesis' obser-

⁴In the paper by Fürst et al. (2018) the naming of the CRSFs is inverted to the naming in this thesis: they use CRSF1 $\hat{=}$ 50 keV and CRSF2 $\hat{=}$ 35 keV.

Table 1: Overview of most significant observations of GX 301–2. Where required, luminosities were calculated from fluxes assuming $d = 3$ kpc. φ denotes the orbital phase.

Paper	Instr.	Year	Exposure	φ	L_{37}	E band
Kreykenbohm et al. 2004	<i>RXTE</i>	2001	200 ksec	≈ 0	< 0.208	2 – 10 keV
Suchy et al. 2012	<i>Suzaku</i>	2008	10 ksec	0.19	0.176	
		2009	60 ksec	0.38	0.343	
Fürst et al. 2018	<i>NuSTAR</i>	2014	38.2 ksec	0.55	0.189	5 – 50 keV
		2015	35.7 ksec	0.75	0.279	
Zalot 2021 (this thesis)		2020	48.5 ksec	0.97	1.696	5 – 50 keV
					0.479	2 – 10 keV

vation. They analyzed two observations and found two cyclotron lines, which appear to be unrelated: additional to the 35 keV line they found a line with an average line energy of 50 keV. This line has not been found in previous papers. One possible reason for this could be the comparably high spectral resolution of *NuSTAR* at high energies, which enabled the detection of the CRSF feature. In their paper they confirmed the strong phase-variability of the low-energy CRSF while also finding a very weak variability of the newly discovered CRSF. The existence of two cyclotron lines raises concern regarding the model of the accretion column of the source. Since the line energies do not appear to be harmonically spaced they must be formed in different regions with different magnetic field strengths. The main question is: are they formed within the same accretion column? Fürst et al. 2018 provide a quantitative model where both lines are formed within the same accretion column: they argue that the weak pulse-phase variability of the high-energy CRSF is consistent with a non-variable line energy of 49.6 keV. In their model this line is formed near the neutron star surface, whilst the other CRSF line is formed at an altitude of 1.4 km above the surface in a radiation-dominated shock. The variability of the latter CRSF is caused by a Doppler shift of the velocity of the infalling matter. This Doppler shift changes with the viewing angle so that the observed line energy varies below and above its true value.

It is at least noteworthy that both of their observations have comparably low luminosities. It is therefore important to observe the source at higher luminosities to further analyze the pulse-phase dependencies of both CRSFs; this will allow to draw conclusions about the geometry and number of accretion columns in the system. Furthermore, a high-luminosity observation allows to compare the CRSF energies for different mass-accretion rates.

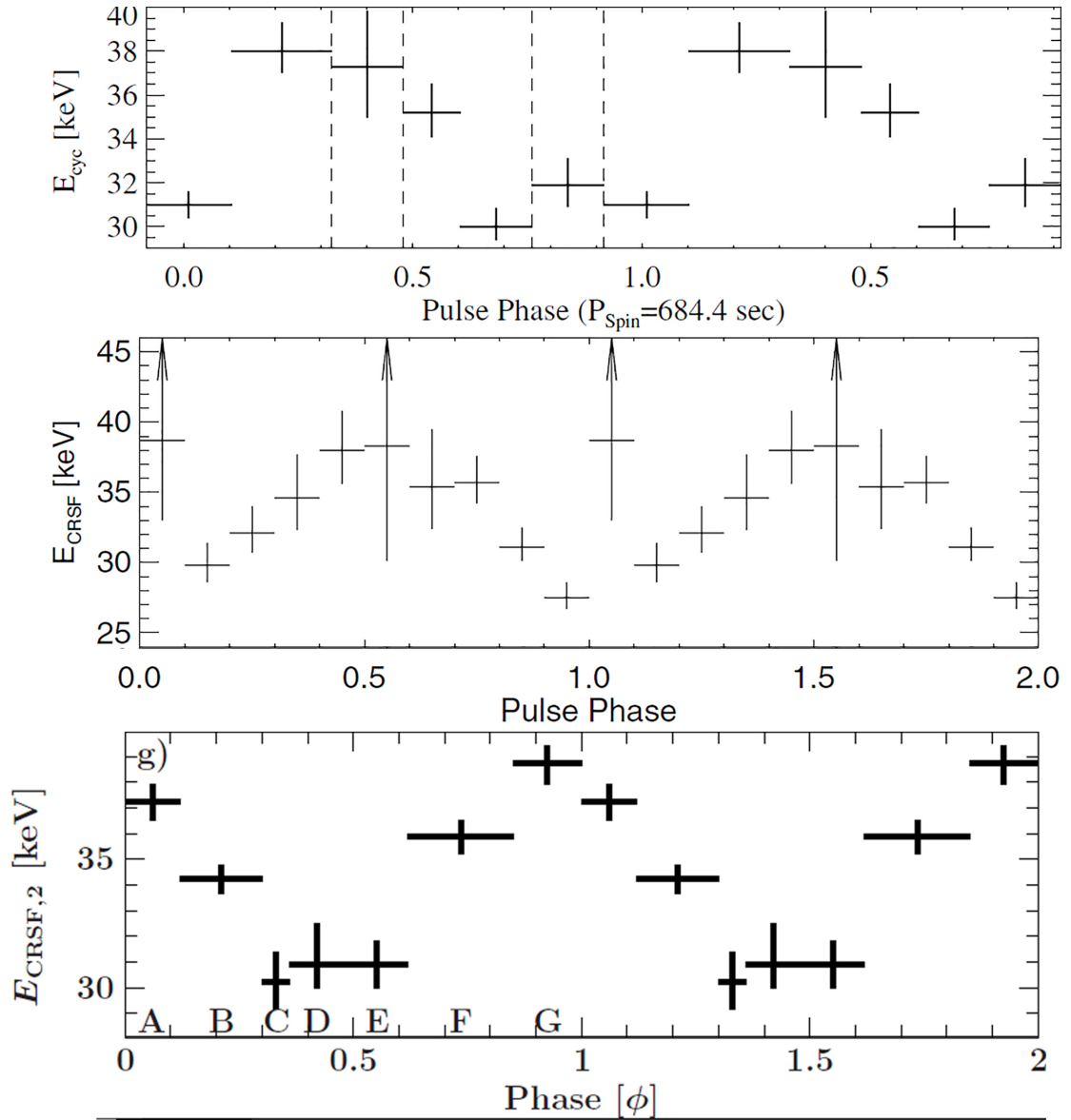


Figure 9: 35 keV CRSF line energy in different papers. From top to bottom: Kreykenbohm et al. (2004), Suchy et al. (2012), Fürst et al. (2018). The phases 0 were not necessarily chosen in agreement with each other.

3.3 *NuSTAR* and its role in CRSF detection

The following provides a brief summary of the *NuSTAR* mission and its advantages for cyclotron line detection. For general information about the mission see <https://www.nustar.caltech.edu/page/instrumentation>; for an in-depth analysis of

NuSTAR and its detectors see Harrison et al. (2013).

The *NuSTAR* (Nuclear Spectroscopic Telescope Array) was launched in June 2012 and is orbiting Earth at an altitude of approximately 650 km. It has an expected orbit lifetime of ~ 10 years. The satellite is equipped with two nearly identical focal plane modules A and B (FPMA, FPMB). *NuSTAR*'s main advantage over other X-ray missions operating in this range is its ability to perform imaging up to energies of ~ 80 keV. With direct imaging, as opposed to coded masks, one is able to obtain source and background spectra separately and can correct for the background in the analysis. Non-imaging detectors on the other hand rely on models for the background spectrum which naturally bring larger systematic errors with it.

Another advantage is *NuSTAR*'s very wide energy range of 3 – 79 keV whilst still having an acceptable energy resolution. A comparison between the effective areas of past and ongoing X-ray missions is shown in Fig. 10. From this figure it is evident that *NuSTAR* is not suitable for high-resolution analysis in the band below 10 keV. However, no other shown instrument can detect X-rays beyond ~ 20 keV. The implications for CRSF de-

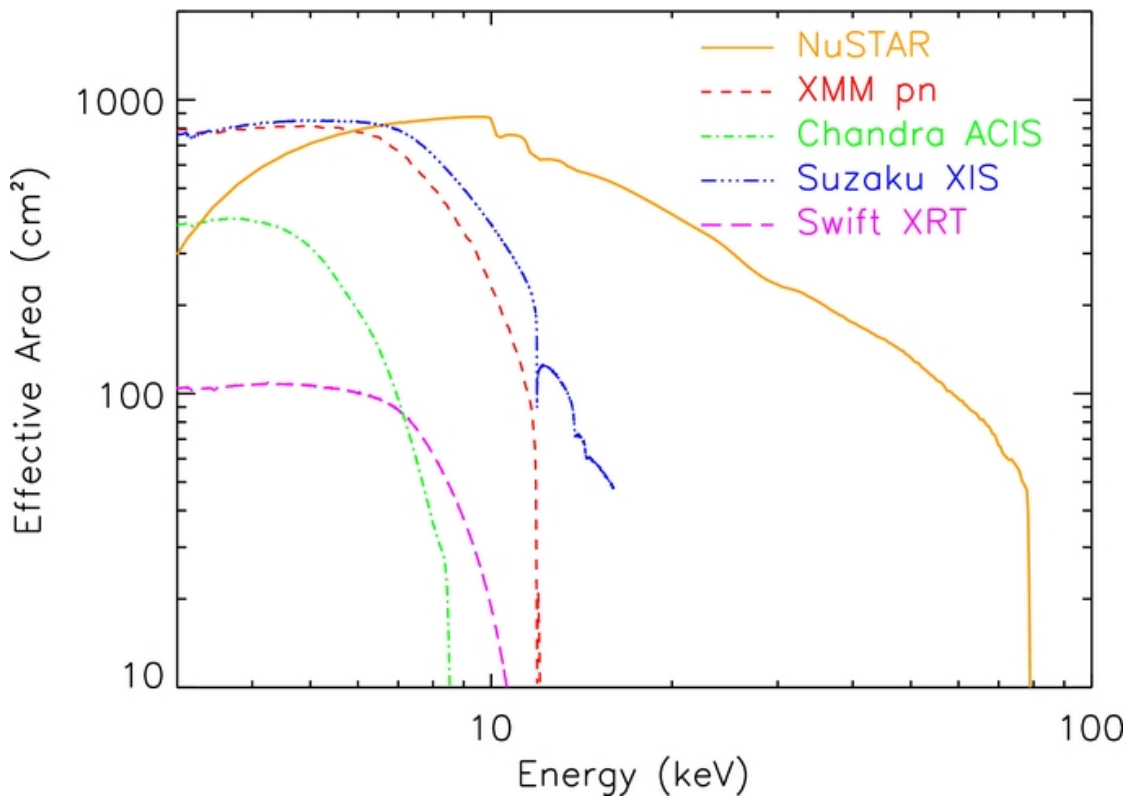


Figure 10: Effective area of *NuSTAR* and other X-ray observatories, Figure 2 from Harrison et al. (2013)

tection by the unprecedented spectral range of *NuSTAR* shall be briefly set out in the

following. Based on Staubert et al. 2019, their Table 1, one finds that cyclotron line energies are usually above 25 keV with the exception of 4U 1626–67 and 4U 0115+63 (see Berger, 2019). From the instruments shown in Fig. 10 only *NuSTAR* can detect X-rays with this energy. However, *Suzaku* has instruments on board which can detect X-rays at 25 keV, e.g. the HXD detector with an effective area of $A_{\text{PIN}}(25 \text{ keV}) \approx 150 \text{ cm}^2$ (see Takahashi et al., 2007). Also, *Integral*'s SPI detector could be used for spectroscopic analysis of the system at hand, albeit with comparably low spectral resolution and without imaging.

NuSTAR's energy range and resolution provides a very good basis for analysis of CRSFs up to energies of $\sim 70 \text{ keV}$. Comparing the effective areas of *NuSTAR* and the *Suzaku* PIN and GSO it is evident that previous studies such as Kreykenbohm et al. 2004 were very unlikely to detect the 50 keV cyclotron line.

3.4 Observation overview

The observation at hand was taken by *NuSTAR* on 2020-12-27. The targeted neutron star in the system GX 301–2 was expected to be close to the periastron at that time. Observations of bright events such as the pre-periastron flare - and high luminosity observations in general - have the advantage that they provide a good statistical basis for spectral analysis compared to low-luminosity observations. Nevertheless, low-luminosity observations do allow for in-depth analysis with statistical significant results, see, e.g., the analysis of neutron star atmospheres by Sokolova-Lapa et al. (2021).

This observation at high luminosity raises the interesting question how the CRSFs behave compared to low-luminosity observations: it is not expected that they appear the same as the conditions in the accretion column change considerably with luminosity.

The exposure times of the observation are 48.5 ksec and 49.0 ksec for the both *NuSTAR* detectors (FPMA, FPMB), respectively. The orbital period of the observation was calculated using orbital parameters by Doroshenko et al. 2010 and is found to be $\varphi = 0.97 - 1.02$.

Unfortunately there were communication problems between the telescope and the ground stations on Earth during the downlink. Because of this approximately 50 ksec of the pre-periastron flare is not recorded. The light curve of the observation is shown in Fig. 11. During the observation the source has an average luminosity on the order of $\sim 1.9 \cdot 10^{37} \text{ erg s}^{-1}$ in the band between 5 – 50 keV. A selection of the most recent *NuSTAR* observations of GX 301–2 and its system characteristics can be seen in Fig. 12. From this figure it is evident that the observation at hand is the only *NuSTAR* observation that aimed to observe the pre-periastron flare.

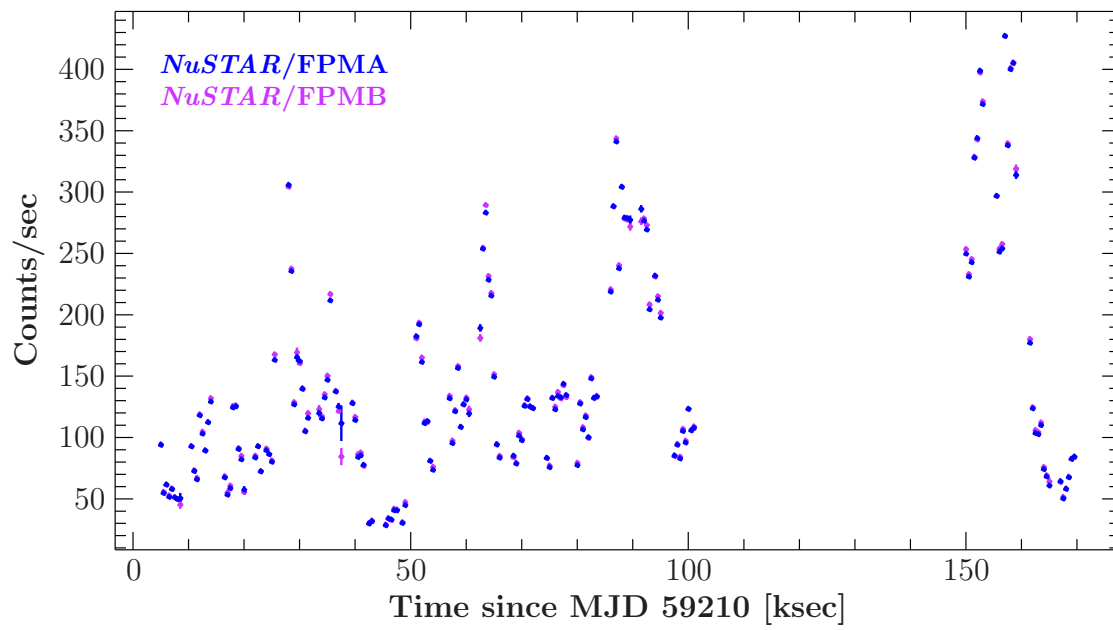


Figure 11: Light curves of both detectors with downlink issues between approximately 100 – 145 ksec. Binning: 500 s.

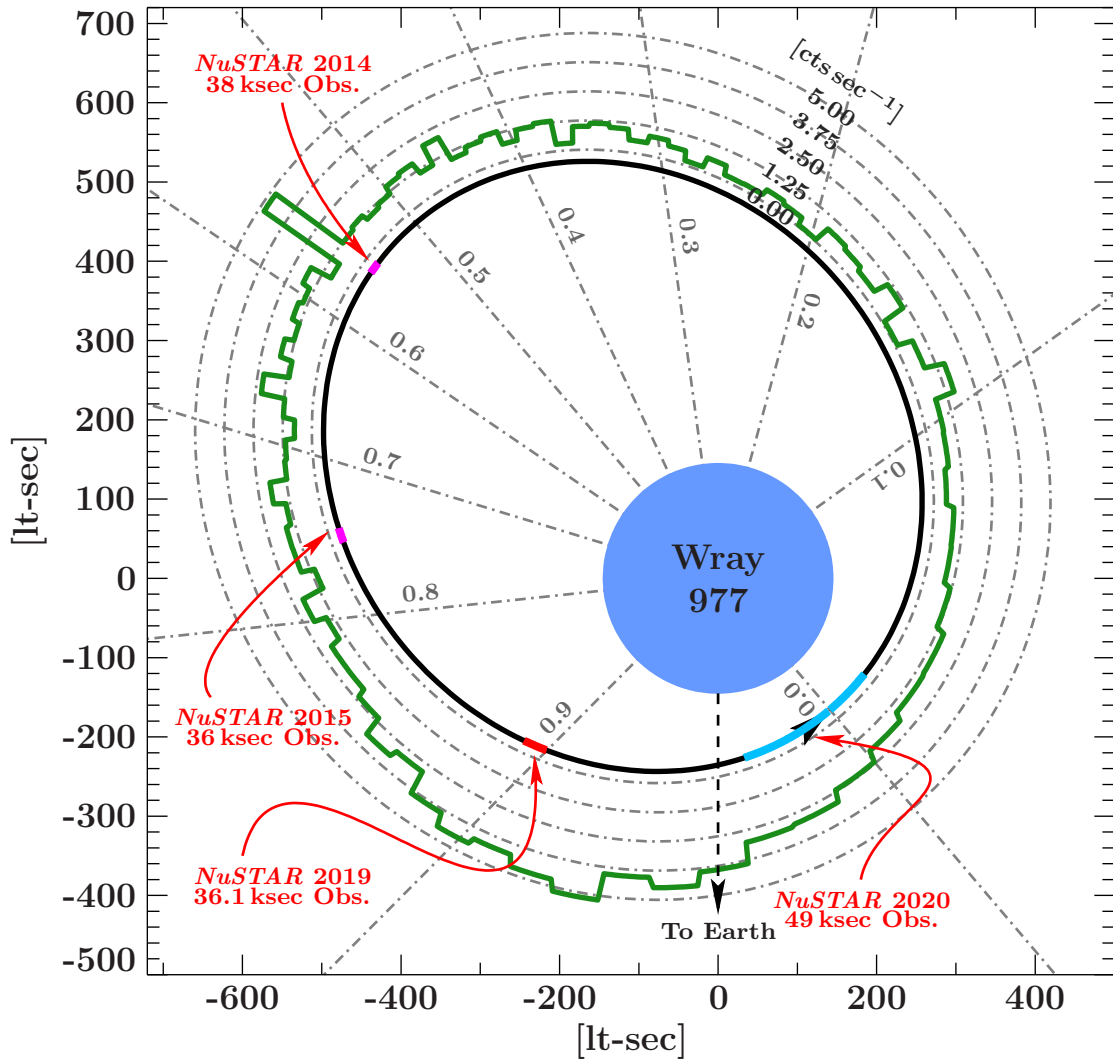


Figure 12: GX 301–2 system with recent *NuSTAR* observations of the neutron star. Figure adapted from Fürst et al. 2011; orbital parameters as in Doroshenko et al. 2010. Shown in black is the orbit of the neutron star, the green graph shows the average RXTE ASM lightcurve.

4 Data processing

In the following section I provide an overview over the data processing required to analyze the spectra.

4.1 Data extraction

The data extraction is done in compliance with the *NuSTAR* Quickstart Guide.⁵ At first, the dataset is spatially inspected to determine the background and source regions. The latter are chosen as circles with radii of 120 arcsec for both detectors, respectively. The radii are chosen as large as possible to maximise the number of source photon events for the following analysis. This generally allows for an analysis with higher precision and better statistics. In the next step the dataset is extracted with `nuextract`, where the raw data is processed so that it is ready to be analyzed with a fitting package. As a part of this processing the photon events are binned into 1 second bins in order to decrease the required hard drive space and speed up routines.

4.2 Data analysis methods

The data analysis of the spectra is conducted using the *Interactive Spectral Interpretation System*, in short ISIS by MIT⁶. It is based on the programming language *S-Lang*, which was developed and is still maintained by John E. Davis. The ISIS environment is mainly used to analyze high-resolution X-ray spectra. ISIS includes many spectral models from XSPEC⁷, which is another X-ray data analysis environment. The main advantage of ISIS is that it offers direct and full programming functionality: this allows for efficient analysis as fitting routines can be partly automated and scripted.

Additionally used were the Remeis ISISscripts⁸, a large collection of ISIS functions which are useful for analysing X-ray spectra. They are maintained and updated mainly by the Remeis observatory scientists.

In combination with Cash statistics the `subplex` algorithm is used to fit model to data. This algorithm needs more time compared to other minimization algorithms. For this reason the Remeis Cluster is used for advanced fitting and uncertainty calculations as the processing time would be on the order of multiple days when using one core.

⁵https://heasarc.gsfc.nasa.gov/docs/nustar/analysis/nustar_quickstart_guide.pdf

⁶<https://space.mit.edu/cxc/isis/>

⁷<https://heasarc.gsfc.nasa.gov/xanadu/xspec/>

⁸<https://www.sternwarte.uni-erlangen.de/isis/>

4.3 Fitting approach

In order to compare a spectral model and observed data quantitatively one needs to account for detector characteristics and other effects which influence the observed spectrum. In ISIS this is done via the forward folding technique: firstly the user specifies a spectral model, which should already describe the data justifiably well. This model is then folded through the response matrix, which is essentially a matrix which simulates how a spectral distribution would be measured by the detector. This response matrix is self-evidently detector-dependent and is usually extracted along with the dataset and already included in the analysis environment. Mathematically⁹, one can describe this procedure as

$$n_{\text{ph}}(c) = \int_0^{\infty} R(c, E) A(E) F(E) dE \quad (13)$$

where $n_{\text{ph}}(c)$ is the source count rate in the channel c , $R(c, E)$ the detector response, $A(E)$ the effective area of the detector and $F(E)$ the photon flux density. A quantized version of this equation is used for data analysis. To obtain the physically interesting quantity $F(E)$ one needs to invert the equation, which is not feasible analytically. For this reason the source flux in one energy bin cannot be directly computed from dataset. After folding the spectra through the response matrix one can compare the observed and simulated spectral model using statistical methods. From this one can improve the fit model to describe the observed spectra better. Within limits, this process can be automated. Nevertheless this is not a programming problem, but a physical one: the parameter starting values and limits need to be chosen carefully and also in consideration of possible parameter correlations and degeneracies. Also, parameter dependencies should be set up where required or reasonable. One example for this is freezing the line energies of prominent emission lines relative to one another; e.g., for Fe K α and Fe K β since their line energies are very well known from atomic physics.

A direct consequence of forward folding can be seen when fitting emission lines with widths of ~ 0.3 keV: changing the width parameter in the model from 0.3 keV to 10^{-6} keV does not change the model or the goodness of the fit, because the very narrowly modelled line is widened by the response matrix to the width of the energy resolution at that energy. Thus it may be useful to freeze certain model parameters since their exact value cannot be determined because they get smeared by the energy resolution of the detector. In this observation this mainly influences the iron lines in the interval between 5.5 – 7.0 keV.

⁹The following equations are given as in lecture notes of “Introduction to X-ray astronomy”, 2018 by J. Wilms.

4.4 Data reduction

Initially the dataset is rebinned to satisfy a minimal signal-to-noise-ratio (S/N) condition of $S/N > 4$. As a result of this, data points for which the criterion is not met are disregarded. Due to the few number of photon events at high energies, this leads to a decrease in spectral range: only up to energies of ~ 60 keV is the S/N criterion met.

The reduced spectral range leads to problems at the inspection of the 50 keV CRSF: due to the lack of data above 60 keV the fitting routines fail to constrain the parameters of the CRSF feature as it interferes with the continuum model parameters. For this reason the rebinning routine is adapted: the data is reduced using the `rebin_dataset_optimal` command, which rebins the dataset in a sophisticated way which follows the formalism by Kaastra & Bleeker (2016). This routine essentially rebins the dataset with respect to many relevant quantities such as the energy of the bin and the effective area of the detector at this energy. With this routine, the usable spectral range of the observation increased to ~ 80 keV.

Using the optimal binning routine has consequences regarding model evaluation: normal signal-to-noise ratio rebinning algorithms assume Gaussian-distributed uncertainties of flux values. In this case, χ^2 statistics are a valid method of testing the goodness of fit, since the χ^2 value of a test function $f(x)$ is defined as

$$\chi^2 = \sum_i^N \frac{(y_i - f(x_i))^2}{\sigma_i^2} \quad (14)$$

where y_i denotes the flux observed in bin i , $f(x_i)$ the fit model evaluated in the bin i with bin middle x_i and σ_i^2 the Gaussian variance of the flux in that bin.

The assumption that uncertainties of observed fluxed are Gaussian-distributed is only valid in bins with enough events so that the difference between the Poisson and Normal distribution are sufficiently small; as a rule of thumb a few 10s of events do suffice. In the bins at high energies this criterion is not necessarily met.

Therefore, Chi-Square statistics cannot be used to analyze the fit statistics for the whole spectral range, as the uncertainties at high energies are not Gaussian-distributed. One therefore uses Poissonian uncertainties, which are much closer to the physical reality: the photon flux is a Poisson process. The three conditions for a Poisson process are easily verifiable in this case: the photon arrival rate is known, the events are discrete and the exact arrival time of a single photon is not known.

By using Poissonian instead of Gaussian uncertainties the Chi-Square statistic cannot be used for evaluating the goodness of the fit. For this reason Webster Cash proposed a different likelihood test: the Cash statistic. The properties of this statistical value will be discussed in the following section.

4.5 Cash statistics

The Cash distribution is given as

$$S_{\text{cash}} = 2 \sum_i^N (f(x_i) - y_i) + y_i \ln \left(\frac{y_i}{f(x_i)} \right) \quad (15)$$

with the same variable definitions as in equation 14.

Cash statistics works better at very low count/bin rates. This can be seen in Fig. 13: for high count/bin ratios both statistics are very similar, but for low count rates they both broaden significantly. In the latter case the Cash statistic reaches its minimum at the point where the guessed counts value equals the true counts value. This is not true for the Chi-Square statistic, where the minima are systematically shifted. A detailed

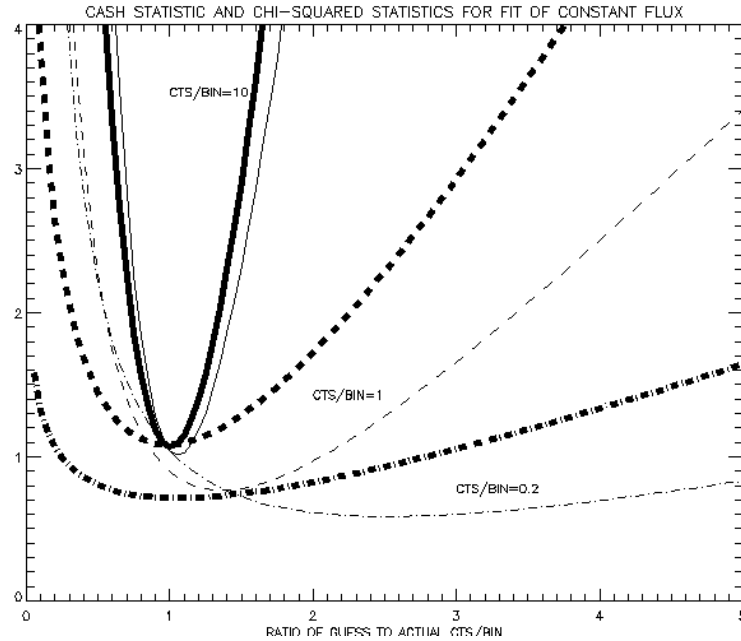


Figure 13: Cash statistics (thick lines) versus Chi-Square-Statistics (thin lines) for different count/bin ratios. The Y-axis shows the statistical values. Figure taken from Schmahl (2005)

description can be found in Cash (1979). For the purposes of this thesis it is sufficient to know that this likelihood test can be used in bins with very few counts, which is the case at high energies for this observation.

5 Spectral models

In the following section the models which are used for the spectral analysis of both the phase-averaged and phase-resolved spectrum will be briefly introduced. This summary includes brief physical motivations but also focuses on the technical implementation in ISIS.

5.1 Continuum models

In this thesis the continuum models used for fitting spectra are of empirical nature. That means that they are only indirectly connected to the physical processes that make up the spectrum, but are rather a description of the spectrum based on mathematical functions with only limited relation to physics.

Since there are physical models for neutron star spectra a justification for using empirical models instead is required: since the main focus of this thesis is not the continuum model itself but the absorption features of the continuum, it is sufficient to use empirical models as the continuum parameters are not of great interest in this work. Furthermore, empirical models pose the advantage that they are very well understood, parameter correlations are comparably easy to find and that they do not require excessive amounts of processing power. Lastly, the available physical models are not sufficiently advanced yet for many scientific purposes; therefore the use of empirical models is justified.

In this thesis three different continuum models will be used and the best of them chosen for the phase-resolved analysis. These three models are the same as used by Fürst et al. (2018). The different spectra produced by the models are shown in Fig. 14. From this figure it is evident that the models produce different result when using identical α and E_{fold} values. This implies that the parameters definitions of the different models are not necessarily identical. One thing the three models do have in common is that they are all based on a power law with exponential cutoff. In the following, the three models will be briefly introduced; a more in-depth description can be found in Müller (2013). The NPEX model was first introduced by Mihara et al. (1995), the FDcut model by Tanaka (1986). The here provided mathematical definition of the `cutoffpl` model can be found in the XSPEC manual ¹⁰.

As mentioned in the preceding sections the continuum part of the spectrum of an accreting, highly magnetized neutron star at high luminosity can be described by a powerlaw and a very steep cutoff at high energies. The simplest model to describe this is a powerlaw with an exponential cutoff. In ISIS this model is called `cutoffpl`:

$$I_E = K \cdot E^{-\Gamma} \cdot \exp \left[-\frac{E}{E_{\text{fold}}} \right] \quad (16)$$

¹⁰XSPEC manual: <https://heasarc.gsfc.nasa.gov/xanadu/xspec/manual/XspecManual.html>

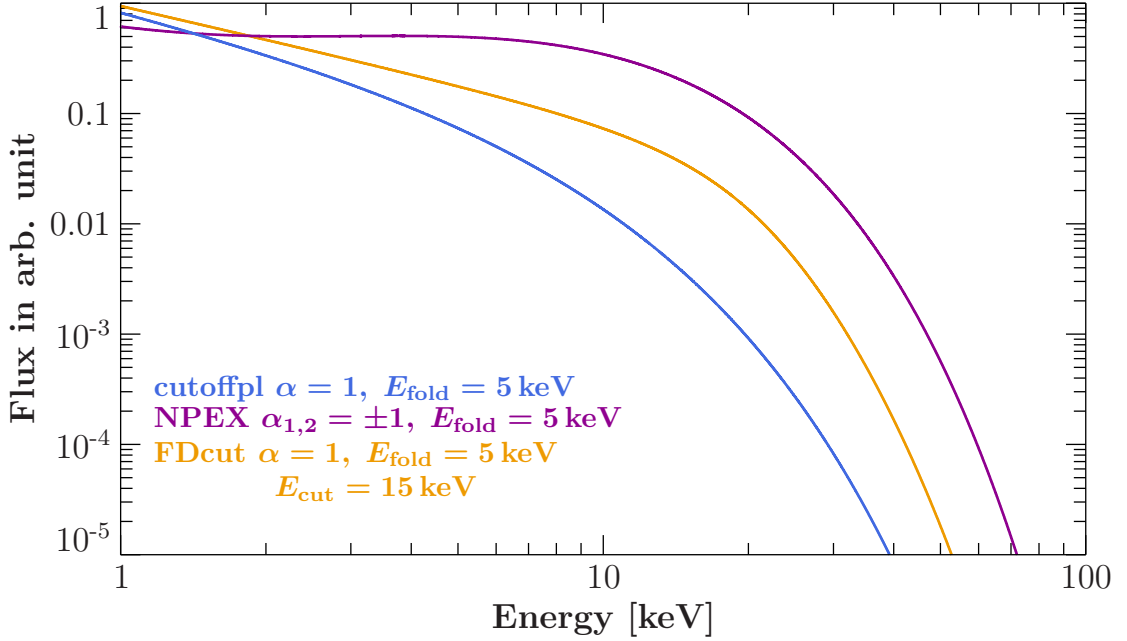


Figure 14: Comparison of the three used continuum models.

This model has only three free parameters: the norm K , the photon index Γ and the folding energy E_{fold} , which determines the slope of the cutoff. Another continuum model, which allows to shift the exponential cutoff is the Fermi-Dirac form of the cutoff with a multiplicative powerlaw component. It can be implemented in ISIS using `powerlaw × fdcut`. Its mathematical expression is

$$I_E = K \cdot E^{-\Gamma} \cdot \left[1 + \exp\left(\frac{E - E_{\text{cutoff}}}{E_{\text{fold}}}\right) \right]^{-1} \quad (17)$$

The additional parameter E_{cutoff} shifts the cutoff energy. In the paper by Fürst et al. (2018) both of these models did not provide satisfying fit results. The model with the best results was the NPEX model, which consists of two powerlaws with a exponential cutoff. One of the photon indices is positive, the other negative. This model can be constructed using two additive `cutoffpl` models with tied folding energies: `cutoffpl × cutoffpl`. Writing this out in mathematical terms yields

$$I_E = K_1 \cdot (E^{\Gamma_1} + K_2 \cdot E^{-\Gamma_2}) \times \exp\left[-\frac{E}{E_{\text{fold}}}\right] \quad (18)$$

This model has in total five free parameters, making it the most adaptive model introduced here. It is noteworthy that the definition given here implies that the parameter K_1 is the total norm of the model whilst K_2 is the norm of the positive powerlaw relative to

K_1 . A value of $K_2 = 1$ therefore implies that the positive and negative powerlaw have the same norm. Furthermore, $\Gamma_2 = 2$ is often used to account for the “Wien proportion of the thermal distribution” (see Staubert et al., 2019, Sec. 3).

5.2 Emission lines

When inspecting the spectrum of the neutron star in the system GX 301–2 the most prominent non-continuum feature is the iron K-alpha line at $E \approx 6.4$ keV. Also a weaker iron K-beta line at approximately 6.9 keV can also be found. Both lines are modelled using the egauss model, which is a Gaussian peak with variable line energy, width and area.

These two features cannot describe the “iron complex” between 5 – 7 keV satisfactory. For this reason a third Gaussian feature with a fixed width of 0.5 keV is added. This has no direct physical justification, but merely serves the purpose to model the data in this region sufficiently well. There are two reason why no more sophisticated, physical models are used to describe the data in this region: firstly, this region is not of primary interest of this thesis, since the main focus are the cyclotron resonant scattering features which mainly influence the spectrum at energies between 30 keV and 60 keV and are not correlated with the iron emission lines. Secondly, *NuSTAR*’s energy resolution at this energy range is not high enough to resolve more refined spectral features. For a analysis of the iron complex of GX 301–2 see e.g. Watanabe et al. (2003).

5.3 Absorption in the interstellar medium

Absorption in the interstellar medium (ISM) is caused by gas clouds and other material that is positioned between the X-ray source and the observer. Since the interaction cross section strongly depends on the ISM composition and the X-ray energy, this absorption does not reduce the flux by a constant fraction, but can rather change the shape and slope of the spectrum. It is necessary to take this absorption into account before analysing the spectrum. In Wilms et al. (2000) routines to model the absorption of X-rays in the interstellar medium are further discussed; the following brief discussion serves as a short summary of their simplest model.

The absorption of electromagnetic radiation between source and observer depends on the optical depth τ . They relate via

$$I(E) = I_0(E) \cdot \exp[-\tau(E)] \quad (19)$$

where $I(E)$, $I_0(E)$ are the observed and emitted intensities, respectively. The optical depth can also be expressed as the product of the total photoionization cross section σ_{ISM} and the number density of the absorber N . The latter has a dimension of cm^{-2} and is a measure of how much absorbing material is between source and observer. Inserting

this into equation 19 yields

$$I(E) = I_0(E) \cdot \exp[-N \cdot \sigma_{\text{ISM}}(E)]. \quad (20)$$

To determine the exponent of the equation in a simple way, Wilms et al. 2000 follow the general convention to normalize the chemical abundance of the ISM to the total hydrogen number density N_H . The total photoionization cross section is in this case given as the sum of the cross sections of the elements weighted with their abundance. Along with neglecting ionization stages, this yields

$$\sigma_{\text{ISM}} \propto \sum_i^{i \in \text{Elements}} \sigma_i \cdot \frac{N_i}{N_H}. \quad (21)$$

Usually, only elements up to $Z = 30$ are included in these models as the abundances of heavier elements is vanishingly small. The detailed equations for the normalized cross sections can be found in equations 3-5 of said paper. This approach also implies that one needs to assume a chemical composition of the ISM in advance. In this thesis, the solar abundances by Anders & Grevesse (1989) are used; the used photoionization cross sections are set to the values given by Verner et al. (1996). Lastly, one can use the following equation with only one fit parameter to model the absorption by the ISM

$$I(E) = I_0(E) \cdot \exp[-N_H \cdot \sigma_{\text{ISM}}]. \quad (22)$$

This model is implemented in ISIS under the name `tbabs`. A slight adaption of this model is used in this work: `tbnew_feo` additionally allows to change the abundances of iron and oxygen.

5.4 Absorption near the source

Absorption near the source itself can also significantly influence the observed spectrum. In this case material near the source absorbs parts of the radiation and thereby affects the observed spectrum. In the simplest case all radiation gets absorbed to the same extent, which can be modelled using routines as described in the previous section.

In other not rarely occurring cases not all radiation is absorbed with the same strength. This can be due to a partial covering geometry. This brief description of partial covering provides a summary of the corresponding chapter in Ballhausen (2021), where a detailed description can be found. Partial covering absorption is caused by inhomogeneities in the material surrounding the source. An illustration of this is shown in Fig. 15. From this figure it is evident that the observed spectrum is significantly influenced by the difference in absorption strength for different optical paths. For two X-rays with identical initial intensities I_0 but different optical depths τ_1, τ_2 the total observed intensity is given by

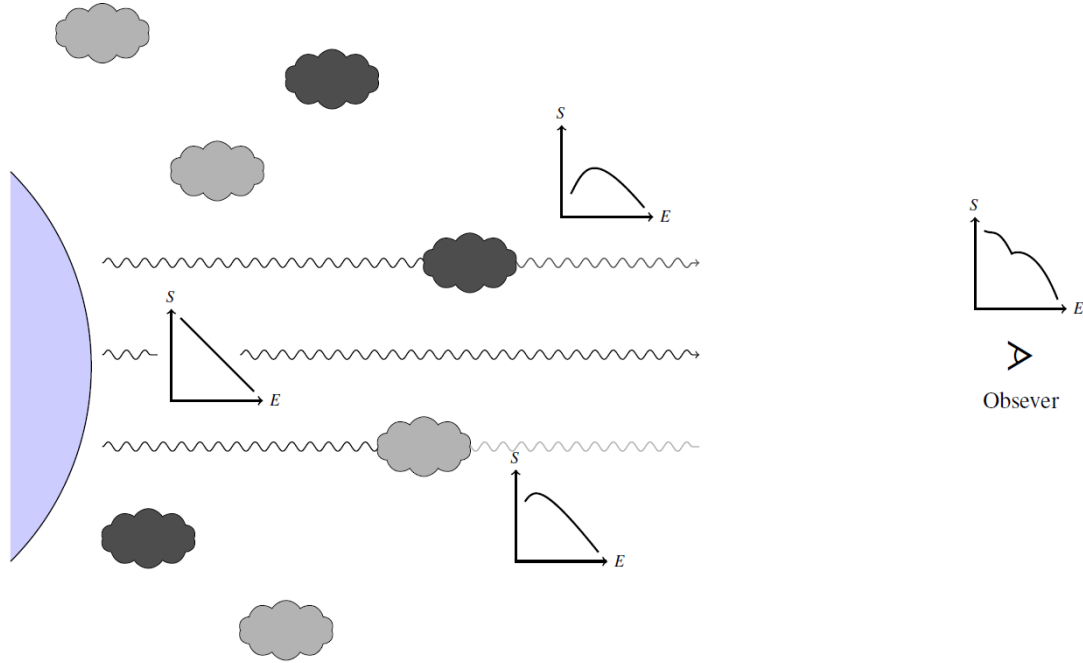


Figure 15: Illustration of a partial covering, which absorbs X-rays differently strong. This leads to spectra that cannot be described by a regular absorption model such as `tbabs`. Figure from Ballhausen (2021).

$$I_{\text{obs}} = I_0[k \cdot \exp(-\tau_1) + (1 - k) \cdot \exp(-\tau_2)] \quad (23)$$

where $k \in [0, 1]$ is the partial covering fraction. This equation cannot be simplified any further; implying that it is not possible to describe the absorption process near the source with one absorption model alone as it requires the combination of two absorption models.

One therefore needs to use a model which reproduces the absorption described in equation 23. In ISIS this can be done by combining two absorption models:

$$I(E) = \text{constant} \times \text{tbnew_feo1}(E) + (1 - \text{constant}) \times \text{tbnew_feo2}(E) \quad (24)$$

The absorption model used in this thesis is a simplified version of the models introduced in this and the previous section: one can include the absorption in the ISM in the model given above. The resulting model is of the form

$$I(E) = \text{constant} \times \underbrace{\text{tbnew_feo1}(E)}_{\text{ISM + Par. cov. term 1}} + (1 - \text{constant}) \times \underbrace{\text{tbnew_feo2}(E)}_{\text{ISM + Par. cov term 2}} \quad (25)$$

5.5 Cyclotron lines

Cyclotron lines can be modelled as absorption features. In many cases apparent absorption features are more complicated to model than emission lines since they are affected by the continuum and cutoff parameters. For GX 301–2 especially the constraint of the cyclotron lines near the exponential cutoff is very difficult.

In this thesis cyclotron lines will be described using the gabs model. This is an absorption line with a Gaussian optical depth. It is defined as

$$M(E) = \exp \left\{ -\frac{d}{\sqrt{2\pi\sigma^2}} \cdot \exp \left[-\frac{1}{2} \cdot \left(\frac{E - E_{cyc}}{\sigma} \right)^2 \right] \right\}. \quad (26)$$

This model does not account for harmonics, which could be modelled by extra gabs models. The inclusion of harmonics is not expected to be required in this thesis for different reasons: the first harmonic of the 35 keV cyclotron line has an energy of ~ 70 keV where the spectrum is already massively dominated by the exponential cutoff. Furthermore, the energy resolution of *NuSTAR* is very low compared to its spectral resolution at the fundamental line energy (see Fig. 10).

The first harmonic of the 50 keV cyclotron line has an expected line energy of ~ 100 keV which lies outside of *NuSTAR*'s spectral range (again see Fig. 10). Furthermore, the exponential cutoff impedes the detection possibility of cyclotron lines at energies where the cutoff dominates the spectral shape. The reason for this is that the parameters of the absorption features cannot be disentangled from the cutoff and continuum parameters as they would strongly interfere with one another. A common solution for this is to freeze the width of the absorption feature, which can allow the determination of the CRSF energy and depth.

5.6 Other spectral components

Additional to the previously introduced models other model components need to be added to describe the spectrum sufficiently well.

In the following study the datasets measured by both detectors FPMA and FPMB will be analyzed together. There are small flux cross-calibration uncertainties between the two modules FPMA and FPMB, which are accounted for by a multiplicative factor for FPMB relative to FPMA in the spectral model. Due to the identical design of the two detectors it is expected that the flux deviations are well below 5%. The used ISIS function is called `detconst`.

To account for a soft excess in the spectrum a blackbody model is included. The used model `tbody` is a blackbody spectrum with two free parameters: the norm K , which determines the flux of this component, and the temperature related energy $k_B T$ in keV.

This model is not used in the fits using the NPEX continuum model since it already accounts for thermal emission through its powerlaw with positive photon index.

In previous papers which focused on the *NuSTAR* detectors (see Madsen et al., 2015) a gainshift in slope and offset has been found between the two detectors. This gainshift is corrected for with the `gainshift` model. It accounts for energy calibration uncertainties by changing energy boundaries for channels in the response matrix.

6 Phase-averaged spectroscopy

In the following section the phase-averaged spectrum of GX 301–2 will be analyzed. Of special interest are the cyclotron resonant scattering features. From this point forward the cyclotron line at 35 keV will be denoted as CRSF1, while the cyclotron line at 50 keV will be identified as CRSF2.

The two datasets from FPMA and FPMB are rebinned using the above described routine to 279 and 280 bins, respectively. The energy band between 3.5 – 79 keV is inspected. As mentioned in section 5.1 three different spectral models are compared. The overall best model will be used in the further analysis of the dataset. The complete fit model is of the form

$$\text{detconst} \times [\text{partial covering absorption} \times (\text{blackbody} + \text{continuum model} \times \text{CRSF1} \times \text{CRSF2}) + \text{Fe K}\alpha + \text{Fe K}\beta + \text{Gauss3}] \quad (27)$$

where the continuum model is either `cutoffpl`, `powerlaw` \times `fdcut` or `NPEX`. The blackbody component is not used in the `NPEX` fits. The phase-averaged spectrum with the mentioned fits can be seen in figures 16, 17 and 18. The parameters of the shown fits are given in the appendix, Table 6.

6.1 Comparison of models

In the following section the three introduced continuum models and the here conducted fits will be compared with regard to their overall quality and how well they constrain the cyclotron line parameters.

6.1.1 Cutoffpl model

The `cutoffpl` model has the simplest form of the exponential cutoff; which is quantified by the folding energy $E_{\text{fold}} = 5.92^{+0.11}_{-0.16}$ keV. In comparison with the other two models it produces the fit of least quality as $C_{\text{red}} = 1.80$ (see Table 3). The residuals at

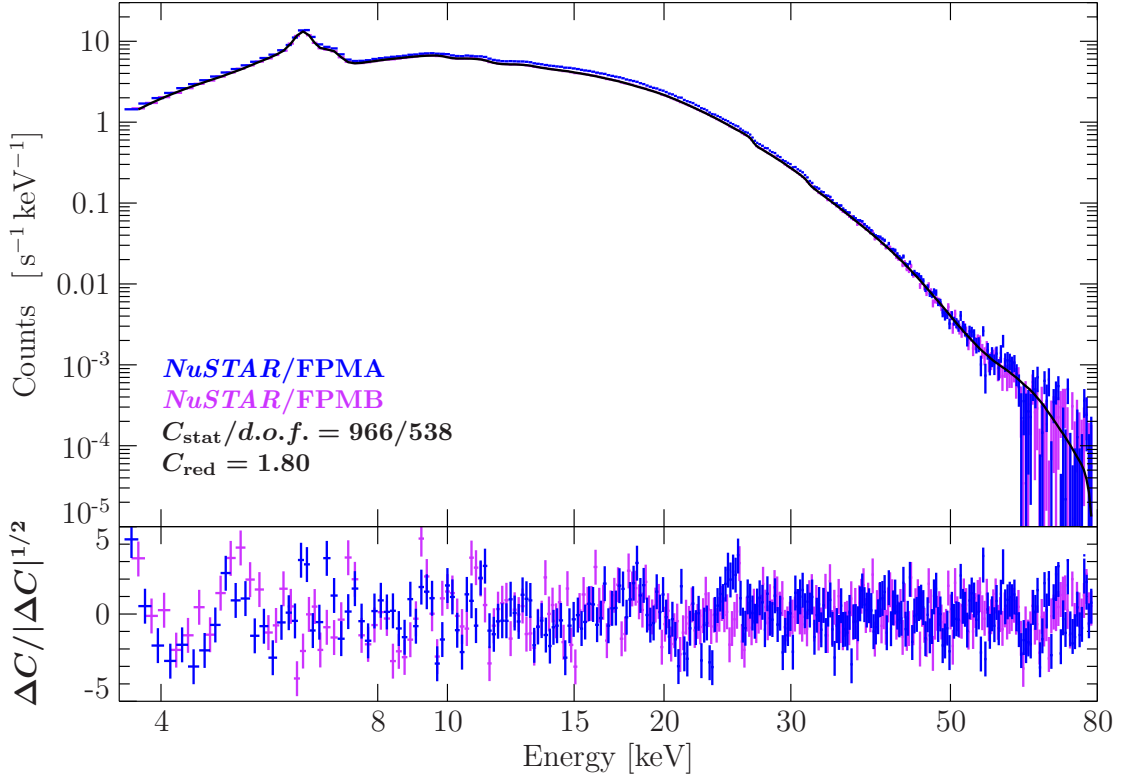


Figure 16: Phase-averaged spectrum with cutoffpl model.

low energies in Fig. 16 appear to be not evenly distributed, but rather wavy. This implies that the model does not account for all spectral features. One reason for this is that the energy band between (4 – 8) keV is only modelled using three Gaussian features. Although the model describes the iron complex rather unsatisfactory I did not try to improve the fits in this region for reasons already previously discussed: the iron complex is not related to the CRSF formation; furthermore *NuSTAR*'s comparably low energy resolution makes the analysis of this region more complicated. For a detailed analysis of the iron complex of GX 301–2 see, e.g., Watanabe et al. (2003). Furthermore the residuals show non-negligible deviations between the two detectors at low energies. At energies above 20 keV the residuals appear to be evenly distributed around the model. Almost all parameters could be constrained within the limits set for the fitting routine. The exception is the depth of CRSF2 with a value of 20_{-4}^{+0} keV, which evidently hits the upper limit of 20 keV. The reason for this could be that the fit algorithm cannot disentangle this parameter from the cutoff parameters and they are therefore correlated.

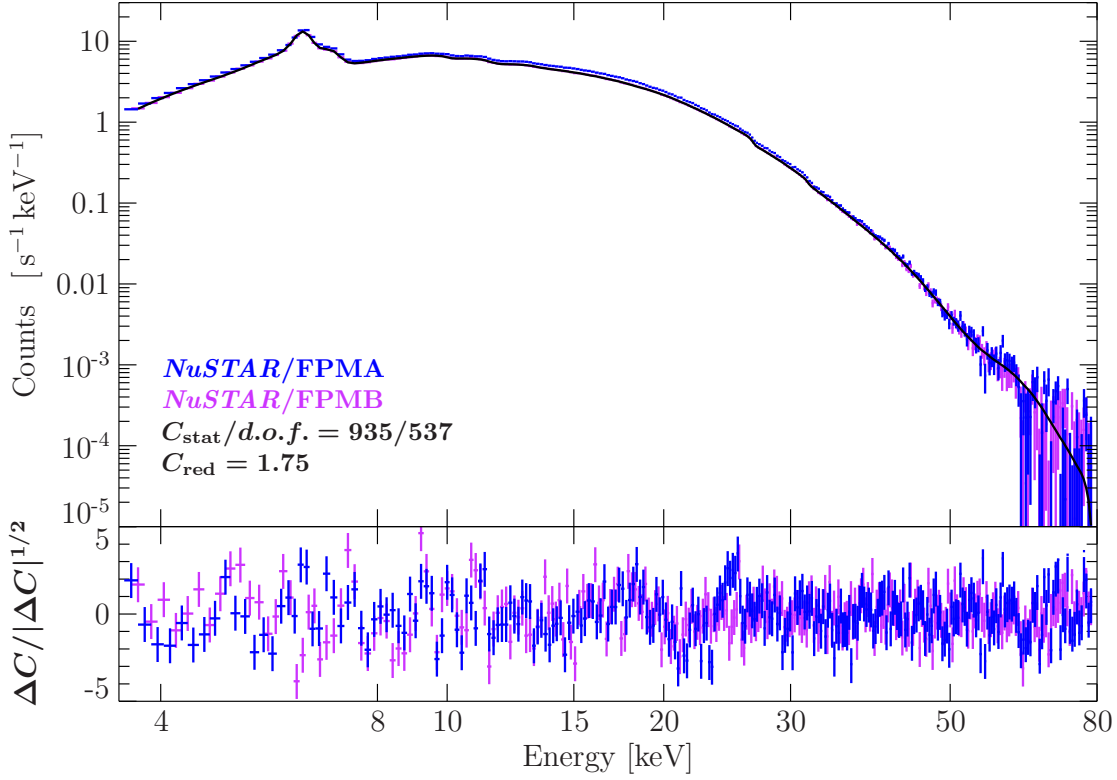


Figure 17: Phase-averaged spectrum with FDcut model.

6.1.2 FDcut model

The FDcut model provides an overall acceptable fit. Nevertheless it has some problems similar to the ones also present in the cutoffpl fit: below 25 keV the residuals also appear to be wavy. In this model the parameters of CRSF2 could be constrained within the limits set. The line energies of both cyclotron lines are in good agreement with the values obtained in the cutoffpl model fit. The additional free parameter of the exponential cutoff model (see equation 17) results in a better modelled cutoff which helps to constrain the depth parameter of CRSF2 to 12^{+6}_{-4} keV.

6.1.3 NPEX model

In terms of statistical comparison, the NPEX model fit describes the dataset similarly well as the FDcut model fit; their absorption and line parameters are in good agreement. This model is able to constrain the depth of CRSF2 to $14.4^{+2.4}_{-1.8}$ keV, which is a better constraint than found by the other two fits. Inspecting the residuals shows similar problems as before at energies below 25 keV. At higher energies the residuals appear to be evenly distributed around the model apart from one dip at $E \approx 60$ keV. The reason for

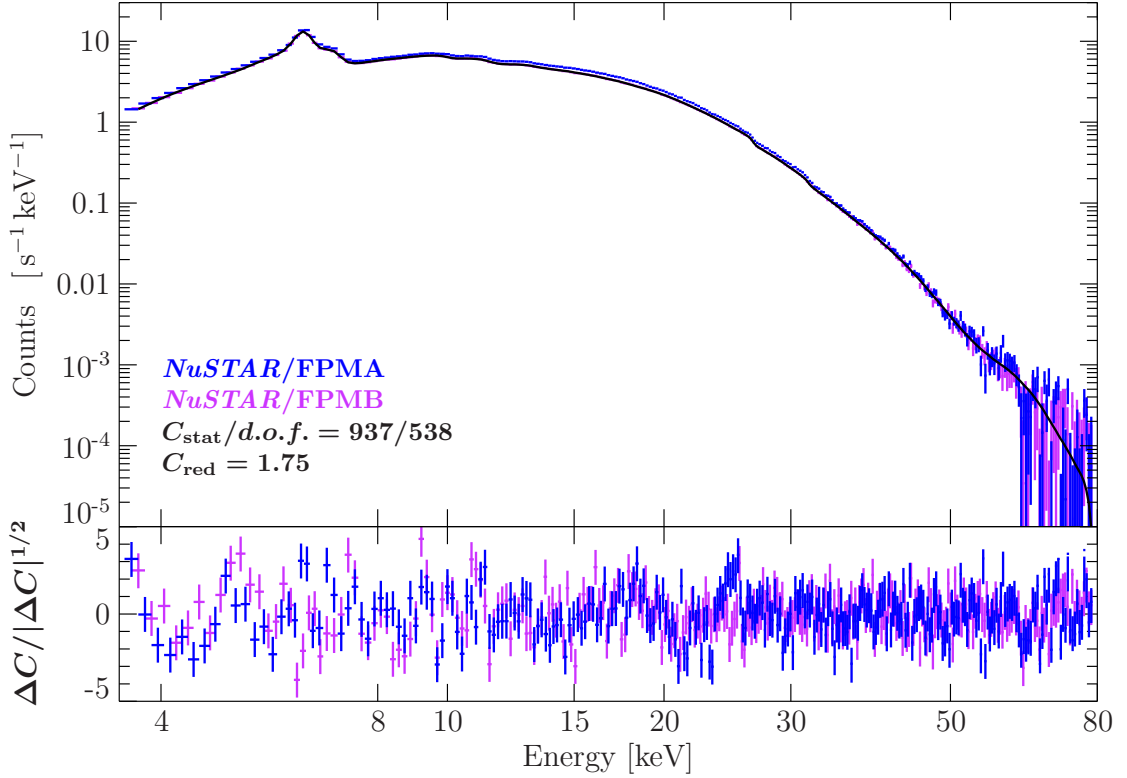


Figure 18: Phase-averaged spectrum with NPEX model.

this could be a combination of *NuSTAR*'s low energy resolution at high energies, the exponential cutoff and incorrect fitting of the 50keV CRSF.

Both the FDcut and NPEX fits describe the data similarly well. One disadvantage of the NPEX model is that its parameters $\tau_{1,2}$ and E_{fold} are often strongly correlated to the centroid energy E_{cyc} of the CRSF feature (see Müller, 2013, 84). The result of this is that the CRSF model component effectively models a part of the continuum and not the CRSF feature. For this reason the FDcut model fit will be used for the following analysis of the phase-resolved spectrum.

6.2 Luminosity of the observation

In theory, the luminosity of the source should not depend on the used continuum model. In my analysis there are slight deviations in luminosity between the used continuum models. This discrepancy is most likely caused by a change in absorption modelling for the different continuum models. Depending on the used model, unabsorbed luminosity values between $(1.79 - 1.96) \cdot 10^{37} \text{ erg s}^{-1}$ were found. This luminosity value is nearly

a whole magnitude brighter compared to *NuSTAR* observations analyzed by Fürst et al. (2018), where luminosities of $(0.1 - 0.3) \cdot 10^{37} \text{ erg s}^{-1}$ were found.

6.3 Cyclotron lines in the phase-averaged spectrum

The cyclotron line at 35 keV has been found in multiple previous observations, e.g. by Kreykenbohm et al. (2004), Suchy et al. (2012) and Fürst et al. (2018) amongst others. The confirmation of the presence of this feature with *NuSTAR* is therefore not the most interesting issue, but rather the phase dependency of its parameters; particularly its line energy as a function of orbital phase as it is closely related to the location of the line-forming region.

CRSF2 has previously only been found by Fürst et al. (2018). To test whether their proposed model for the formation of this line could be true, the line parameters and their phase-dependencies are of special interest for this thesis. Analyzing the existence of this second cyclotron line using statistical means is beyond the scope of this thesis. However, conclusive arguments for or against the existence of the CRSF will be presented in the following.

The first considered criterion is the behaviour of the statistical values for different models with different numbers of cyclotron lines. For this reason the above described models were each fitted with 0, 1 and 2 cyclotron lines. The resulting statistical values are shown in Table 2.

Table 2: Cash-Statistic for different models with and without cyclotron lines.

Model	0 CRSF		1 CRSF (35 keV)		2 CRSF	
	$C_{\text{stat}}/\text{d.o.f.}$	C_{red}	$C_{\text{stat}}/\text{d.o.f.}$	C_{red}	$C_{\text{stat}}/\text{d.o.f.}$	C_{red}
cutoffpl	1983 / 544	3.65	1259 / 541	2.33	966 / 538	1.80
FDcut	1491 / 543	2.75	1163 / 540	2.16	935 / 537	1.75
NPEX	1966 / 544	3.62	1174 / 541	2.17	937 / 538	1.75

All models show significantly improved fit statistics when including both cyclotron lines. This is already an indicator in favour of the existence of both CRSFs, but is not sufficient. To further assess the existence the fitted parameters are analyzed regarding their physical interpretation and validity. The parameters of both cyclotron features can be seen in Table 3, a complete list of the fit parameters are shown in the appendix, Table 6.

Table 3: Parameters of both cyclotron lines in the phase-averaged spectrum for the three shown spectral models and fit statistics of the fits

Parameter [keV]	cutoffpl	FDcut	NPEX
CRSF ₁ line energy [keV]	37.3 ^{+1.1} _{-1.0}	38.6 ^{+1.0} _{-0.9}	38.0 ^{+1.0} _{-0.9}
CRSF ₁ width [keV]	7.7 ^{+0.7} _{-0.6}	8.8 ^{+0.9} _{-0.8}	8.0 ^{+0.9} _{-0.5}
CRSF ₁ depth [keV]	11.3 ^{+2.6} _{-2.2}	12.3 ^{+3.4} _{-2.1}	11.7 ^{+3.7} _{-1.7}
CRSF ₂ line energy [keV]	53.7 ^{+0.7} _{-0.8}	53.4 ± 0.9	53.1 ^{+1.0} _{-0.6}
CRSF ₂ width [keV]	7.4 ^{+0.4} _{-0.8}	5.9 ^{+1.1} _{-0.9}	6.4 ^{+0.8} _{-0.6}
CRSF ₂ depth [keV]	20 ⁺⁰ ₋₄	12 ⁺⁶ ₋₄	14.4 ^{+2.4} _{-1.8}
$C_{\text{stat}}/d.o.f$	966 / 538	935 / 537	937 / 538
C_{red}	1.80	1.75	1.75

The line energy of CRSF1 found by all three models are in good agreement with each other. The 90% uncertainties are well constrained within the limits of (28 – 42) keV. The line energy of CRSF2 could also be well constrained by all three models with uncertainty margins around and under 1 keV. The fitted depths of CRSF1 are in good agreement with each other, although their upper uncertainty intervals are comparably large. The fitting of the depth of the second cyclotron line faces the same problems as discussed for the width of this feature: its proximity to the area where the exponential cutoff dominates the spectrum makes it difficult to constrain this parameter. This can be seen in the value obtained for the *cutoffpl* model, where the value hits its upper limit of 20 keV, which is far stronger than what is expected from the comparably small absorption feature in the residuals, see Fig. 20 panel c. This could be an indicator that the CRSF component models the continuum instead of the CRSF; however, the line energy of the line is fitted in very good agreement with the values from the other two models. In the other two models the parameter could be constrained within the limits, nevertheless the obtained values are also larger than anticipated. To judge whether the fitted widths of the CRSFs agree with the theoretical expected values one estimates an upper limit for the widths using equation 12. A common value for the plasma temperature is $k_B T_e \sim 5$ keV, see, e.g., Becker & Wolff (2007), figures 6,7 and 8. To estimate an upper limit $\theta = 0$ is assumed for the angle between the line of sight and the magnetic field axis. One finds therefore for the 35 keV and 50 keV cyclotron lines

$$\begin{aligned}\sigma_{\text{CRSF1}} &\lesssim 8.2 \text{ keV} \\ \sigma_{\text{CRSF2}} &\lesssim 11.7 \text{ keV}.\end{aligned}\tag{28}$$

Keeping these values in mind as a rather optimistic upper limit for the cyclotron widths the fitted values for the widths will now be analyzed.

The width of CRSF2 is also well constrained by all models. Its value varies between (5.9 – 7.4) keV for the different models, which is well below the estimated upper limit of this line width.

The width of CRSF1 is well constrained by all models. The mean of all models is roughly 8.2 keV which is equal to the upper limited determined above. Given the fact that the estimate is rather generous it is very unlikely that the determined width is the true Doppler-width of the line. On the contrary, there are multiple mechanisms which could cause a broadening of the line, of which one will be illustrated in the following: The broadening of CRSF1 could be caused by a phase variability of the line energy. A strong phase-dependency was previously found by Kreykenbohm et al. (2004) and Fürst et al. (2018) figure 7, panel 7 amongst others. How this phase-variability of the line energy would impact the width of the line in the phase-averaged spectrum is sketched in Fig. 19.

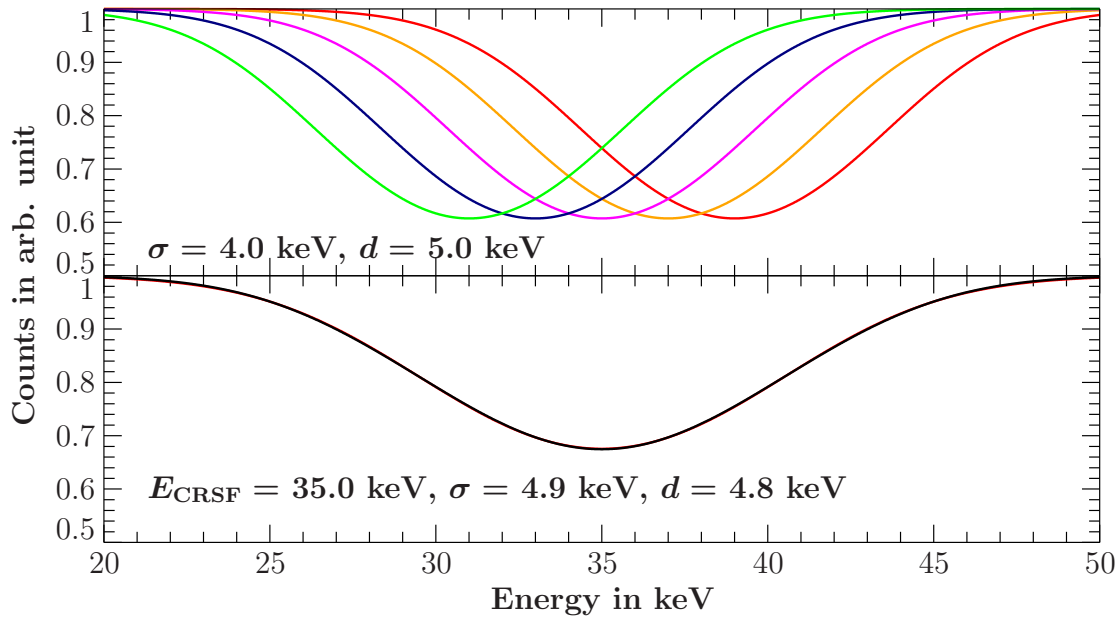


Figure 19: Phase variability of the CRSF energy can result in an artificial line broadening of the line energy in the phase-averaged spectrum. This effect is simulated here by adding up five CRSF features with varying line energies. Top panel: 5 CRSF absorption features modelled with the gabs model with identical widths and depths. The line energies are (31, 33, 35, 37, 39) keV. Bottom panel: normed sum of the above depicted CRSF models (black) with fitted gabs model (red) and fit parameters below.

The depicted absorption lines, which could be found in a phase-resolved spectrum, with widths of 4.0 keV add up to one wider cyclotron line with a fitted width of 4.9 keV. This wider line is the result of smearing and averaging of the narrower lines and would be

found in the phase-averaged spectrum.

Whether this effect causes the wide cyclotron line cannot be determined without inspecting the phase-resolved spectrum (see Sect. 7).

The last means to assess the cyclotron lines of the observation at hand in the phase-averaged spectrum is to analyze the residuals of models with and without cyclotron lines. This is shown seen in Fig. 20. In panel c the residuals of the FDcut model with only CRSF1 are shown. At 50keV an absorption feature is clearly visible, which also indicates the existence of the second cyclotron line. This figure is designed to be directly comparable to Fürst et al. (2018) figure 2, where the same residuals are shown for their best-fit model, which is the NPEX model. In comparison their low-energy fits are significantly better as their residuals are distributed more evenly around the model. The ratio residuals look very similar between both figures.

A more sophisticated tool to analyze the properties of the cyclotron lines is to check correlations between continuum parameters such as the cutoff energy and the CRSF parameters. This is often graphically illustrated with contour plots, which can very easily show correlations of parameters.

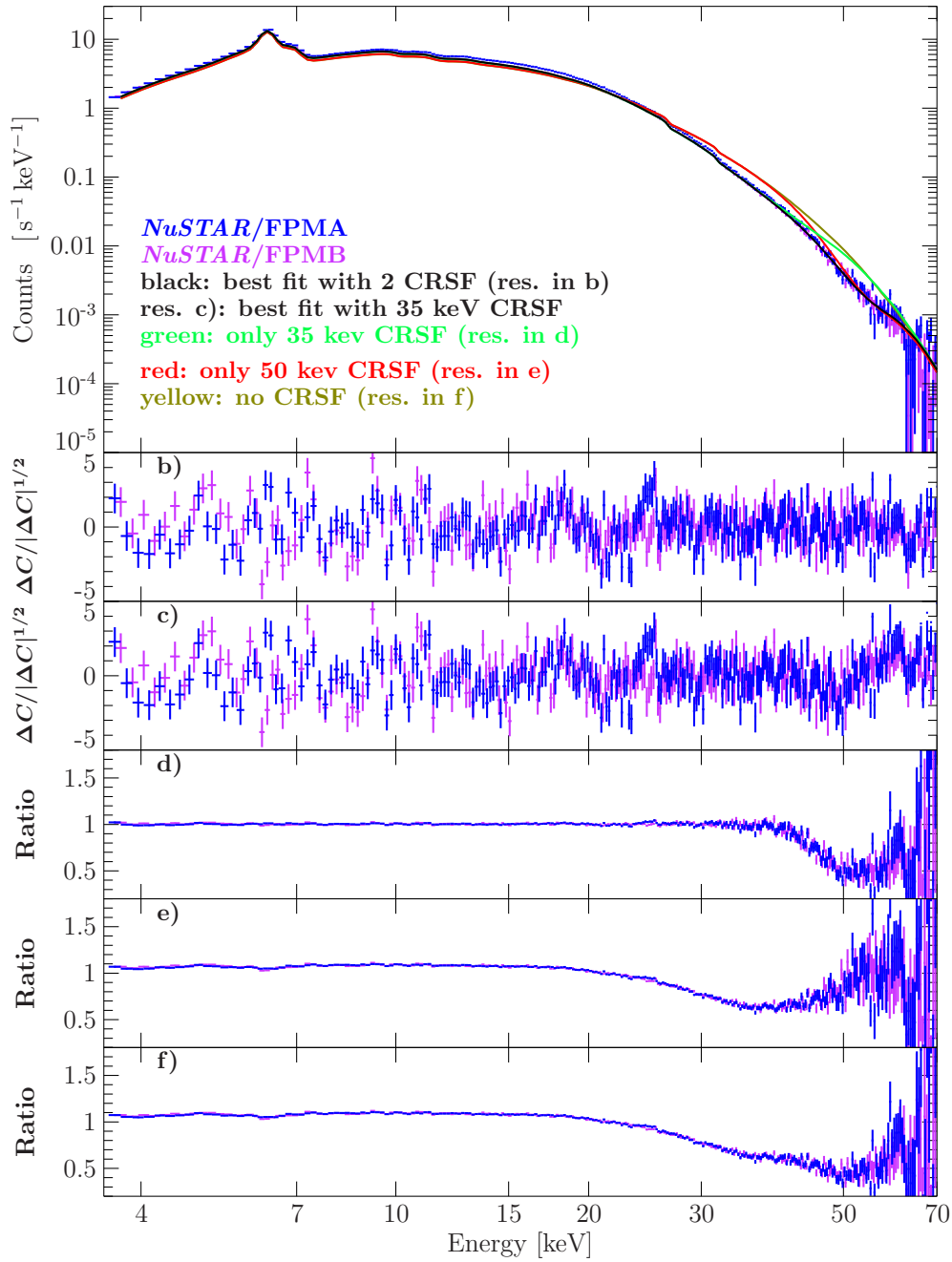


Figure 20: Top panel: data with different models (see legend). Panel b: Residuals of best FDcut fit. Panel c: Residuals of best-fit of FDcut model with only CRSF1. Panel d-f: Ratio residuals of original best FDcut fit with cyclotron lines removed in turns.

7 Phase-resolved spectroscopy

In order to study the accretion column geometry of GX 301–2 one examines the phase variability of the spectral features. Since the accretion flow is dominated by the magnetic field, which also impacts the CRSFs and their energies, the phase-dependence of the cyclotron lines is of special interest. The main focus will be on their line energies and strengths as they are expected to be more phase-dependent than the widths, which are difficult to describe in phase-resolved spectroscopy due to less total counts which hinders the minimization algorithm. Furthermore the widths are not expected to be as phase-dependent as the line energies and strengths. Nevertheless, they can be phase-dependent since the parameter θ in equation 12 is almost certainly phase-dependent, since the magnetic field axis is not necessarily perpendicular to the line of sight.

7.1 Determination of the pulse period

To determine the pulse phase of the emitted radiation by GX 301–2 different functions provided by the `ISISscripts` are used. At first the event files are loaded into ISIS. For the calculation of the pulse period the function `epfold` is used, which is based on the epoch folding technique described by Leahy et al. (1983). This routine estimates the pulse period by using statistical means: it determines the statistical likelihood that a period signal with a given pulse period describes the dataset well. The upper and lower limits of this incremental testing are chosen in consideration of pulse periods determined in other papers on GX 301–2. The pulse period is then determined in 100 steps between 671.2 s and 671.9 s. The uncertainties of the pulse period and its time derivatives \dot{P} and \ddot{P} are not of interest in this thesis, since the pulse period is only required to divide the data into phase bins. The values found are shown in Table 4. This analysis is conducted for both detectors separately to check for significant deviations between the determined pulse periods. Admittedly, this is neither expected nor observed. For the following analysis the average of the determined pulse periods will be used.

Table 4: Determined pulse periods for both detectors and their mean value.

Detector	Pulse period [sec]
FPMA	671.606
FPMB	671.595
Mean	671.601

The difference between the determined pulse periods of the two detectors is most likely a result from statistical and computational problems and not a detector property or a physical feature.

7.2 Phase bin extraction

After determining the pulse period the events of the lightcurve need to be filtered in order to divide them in phase bins. The mask for this filtering is created using the GTI command in ISIS. This filter can then be passed on to the `nuextract` extraction program as an optional argument.

In this thesis the phase will be divided in 10 equally spaced phase bins. Considering the comparably high luminosity of this observation, this is a good trade-off between number of bins and events/bin. Choosing too many bins decreases the events/bin ratio, which leads to difficulties of fitting spectral models in the phase intervalls. Choosing too few bins results in not-significant results when assessing the phase-dependency of the fit parameters.

The pulse profile and the spectral bins are shown in Fig. 21.

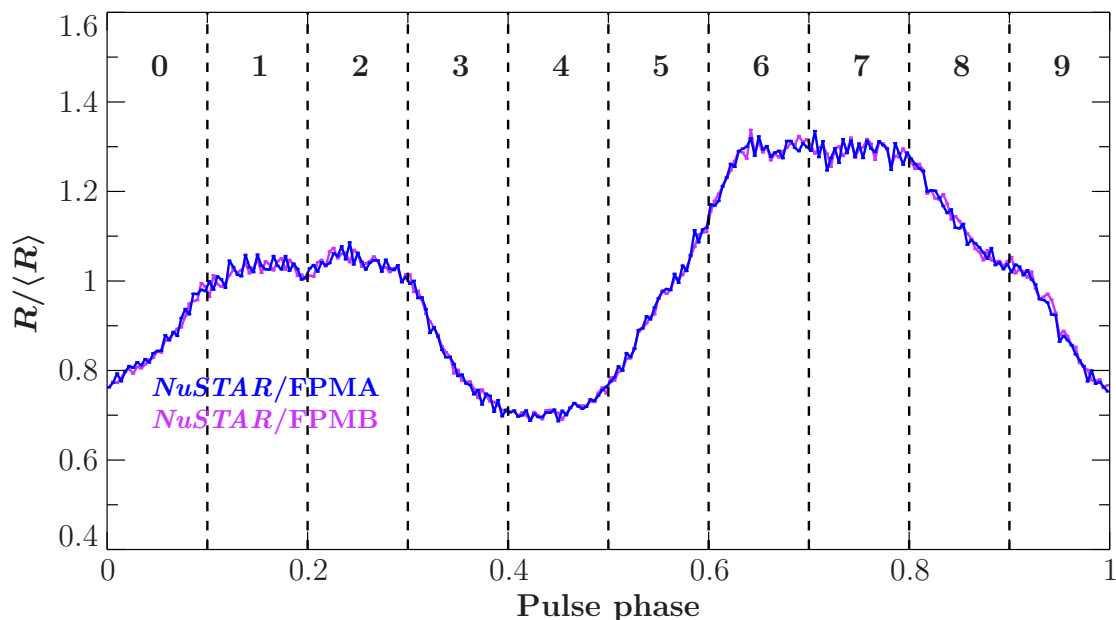


Figure 21: Pulse profile of *NuSTAR* observation of GX 301–2 using 250 phase bins. Dotted lines separate the 10 bins used for the phase-resolved spectroscopy. The count rate R is normed by the average count rate $\langle R \rangle$.

7.3 Spectral analysis

For the spectral analysis of the phase-resolved spectrum the `FDcut` model is used. A preliminary analysis showed that the widths and depths of both cyclotron lines could not be constrained within reasonable limits in each spectral bin. For this reason the widths of the lines are held fixed in the following analysis to ensure that the energies

and depths can be determined in a physically meaningful way. The widths of both lines are chosen with respect to the estimated upper limit, the fitted values in the phase-averaged spectrum and for CRSF2 also the width of the residual dip in Fig. 20, panel c. The following parameters are therefore chosen:

$$\begin{aligned}\sigma_{\text{CRSF1}} &= 5 \text{ keV}, \\ \sigma_{\text{CRSF2}} &= 2.5 \text{ keV}.\end{aligned}\tag{29}$$

These values are partly in contradiction to equation 12, where the proportionality $\sigma_{\text{CRSF}} \propto E_{\text{CRSF}}$ is given. From this relation it is expected that CRSF2 is wider than CRSF1 due to its higher line energy. From the phase-averaged analysis it is evident that this does not appear to be the case: the width of CRSF1 is on the order of 7 – 8 keV. To account for a possible broadening as shown in Fig. 19 a smaller value is chosen. The width of CRSF2 is chosen regardless of the values determined in the phase-averaged analysis, but with respect to the width of the absorption feature in the residuals in Fig. 20. These values do not necessarily reflect the real widths of the CRSFs but serve as a reasonable estimate for the parameters.

The fit statistics of the 10 fits are shown in Table 5.

Table 5: Fit statistics of fitted FDcut model in all spectral bins.

Bin	$C_{\text{stat}} / \text{d.o.f.}$	C_{red}
0	630 / 450	1.40
1	597 / 464	1.29
2	609 / 468	1.30
3	567 / 465	1.22
4	631 / 454	1.39
5	584 / 451	1.30
6	537 / 459	1.17
7	647 / 464	1.40
8	582 / 461	1.27
9	539 / 448	1.21

One reason why $C_{\text{stat}} > 1.0$ for the phase-resolved fits is that the problems at low energies still persist as they are only rudimentarily modeled.

Overall the fit quality acquired here is sufficiently good to analyze the phase-dependency of the model parameters. To further illustrate the quality of the conducted fits their residuals are shown in Fig. 22. From this figure it is evident that in each phase bin the data does not show large deviations from the fit.

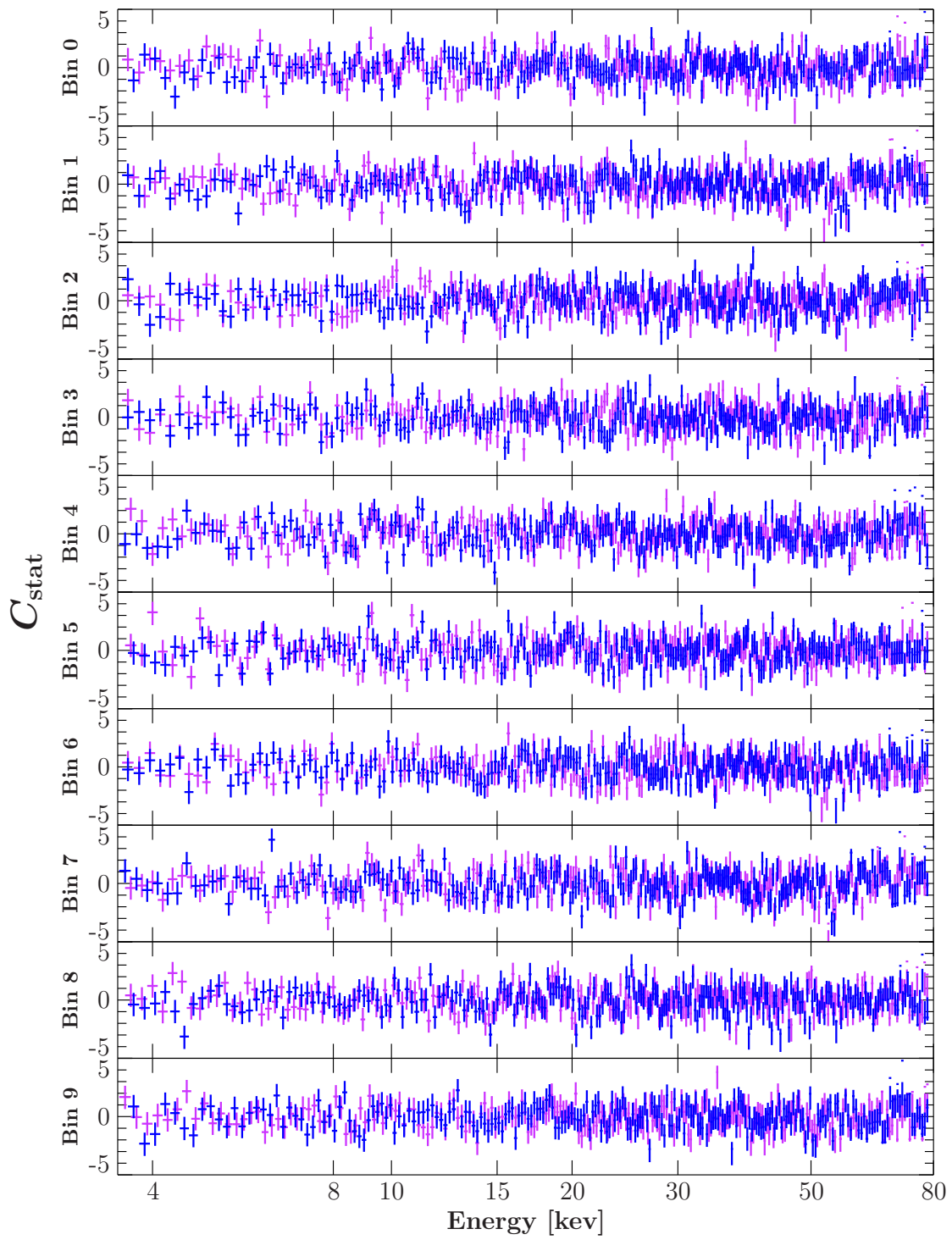


Figure 22: Cash residuals of conducted FDcut model fits in all phase bins.

7.4 Phase dependency of parameters

In the following, the phase dependency of the continuum and cyclotron line parameters will be analyzed (see Fig. 23).

The observed flux of the source varies as expected from the pulse profile (see Fig. 21).

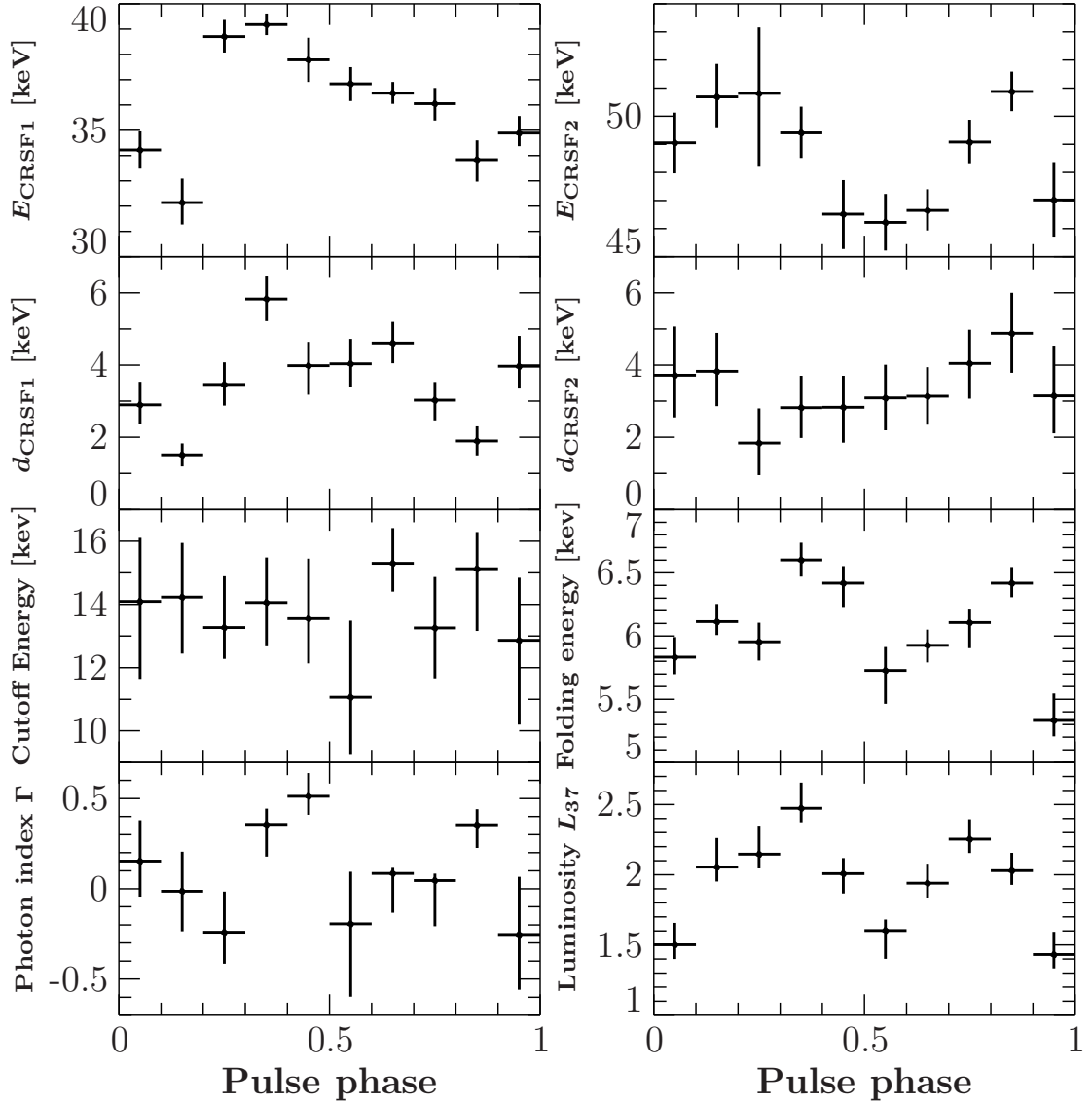


Figure 23: Phase-dependency of continuum and CRSF parameters with 90% uncertainty bars.

From the flux profile a mean luminosity of $\langle L_{37} \rangle = 1.94$ is derived. This value is in good agreement with the luminosities determined by the cutoffpl and NPEX models

in the phase-averaged spectrum, whilst the FDcut model found a lower luminosity of $L_{37} = 1.75$.

The continuum parameters such as the photon index, cutoff and folding energy are expected to show pulse-phase variability due to a change in viewing angle. The rotation of the neutron star can lead to a situation where the observer sees the accretion column from the top and side in turn.

The cutoff energy does not appear to be phase-dependent. It must be acknowledged that this parameter has comparably large uncertainties, which could conceal a small phase dependency.

The folding energy shows significant variations over the pulse phase. Sole examination of the figure suggest a proportionality to the observed flux.

The photon index shows a comparably small phase-dependency which could also be a false positive as the variation is generally smaller than the uncertainty margins of the value itself. The values determined appear to be evenly spaced around the value determined in the phase-averaged spectrum using the FDcut model of $\Gamma = 0.23$.

CRSF1 shows a very strong phase-dependency: its energy varies between (30 – 40) keV. It is highly unlikely that this correlation is caused by bad fitting as the uncertainty intervals are comparably small. The strength of this line also shows some phase-dependency, which is however far smaller.

The cyclotron line at 50 keV also shows phase-dependent variations for the line energy, which varies between (45 – 52) keV. The obtained strength values however are consistent with a non-phase dependent value of approximately $d \approx 3$ keV.

7.5 Impact on the phase-averaged spectrum

In section 6.3 possible explanations for the broad width of CRSF1 in the phase-averaged spectrum were given. One of them is based on a strong line energy variability. Since the line energy of CRSF1 is strongly variable it could be the cause of the broad width in the phase-averaged spectrum. To assess whether this effect alone can create such a wide line the expected line width will be simulated using the parameters acquired from the phase-resolved spectrum. In essence, this is the same simulation as shown in Fig. 19 but using the phase resolved parameters for the different CRSFs. The models are then weighed with the flux of the corresponding phase bin. The result is shown in Fig. 24. From this figure it is evident that the phase-variability of the line energy cannot explain a width of ≈ 8 keV in the phase-averaged spectrum as the fitted width is only 5.4 keV. One possible reason for this could be the fixed width of 5 keV which is not necessarily the real width of the cyclotron feature. To determine the width in both the phase-resolved and phase-averaged spectrum more reliably one could use an observation with higher luminosity: this benefits the minimization algorithm and could enable a phase-resolved fitting without fixing the width beforehand. One would then acquire more accurate cyclotron line parameters which would bring this simulation closer to the

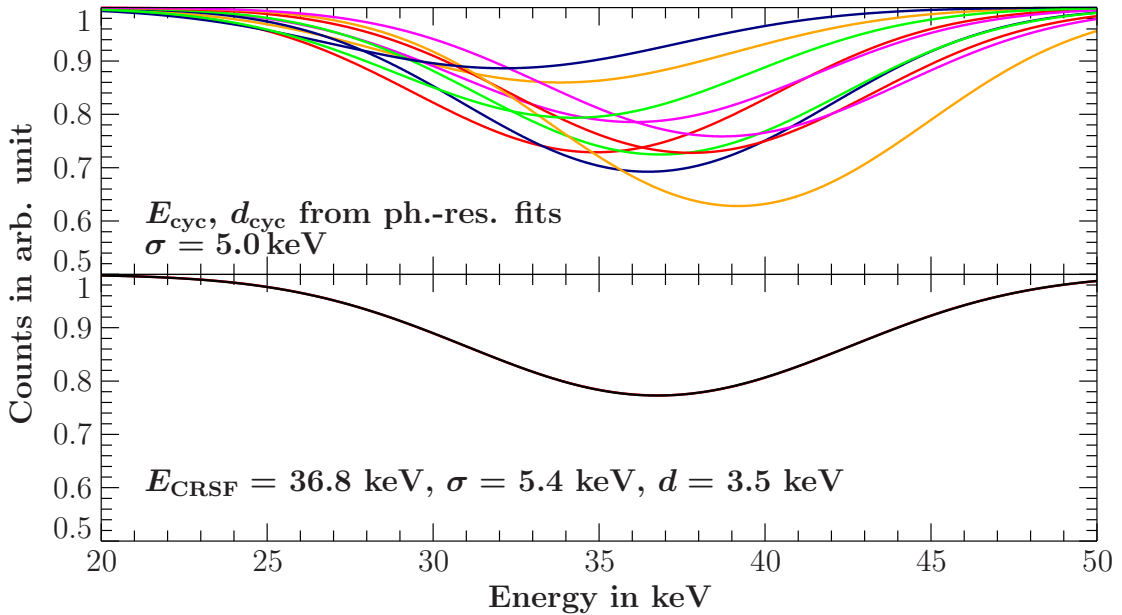


Figure 24: Top panel: cyclotron lines with parameters from phase-resolved fits in 10 phase bins. Bottom panel: mean of top panel lines weighted with the flux in each bin (black), cyclotron line model fitted (red).

physical reality. It is at least noteworthy that this goal could possibly have been achieved without the significant gap during the pre-periastron flare in the dataset. Another possible source of the wide line could be pulse-phase dependencies of continuum parameters such as E_{fold} , which heavily influence the CRSF parameters.

8 Discussion and comparison to previous papers

In this section the results of the analysis will be interpreted in regards to the accretion columns and line-forming regions of GX 301–2.

8.1 CRSF parameters

Both the CRSF parameter values and their pulse-phase dependencies will be discussed and compared to the values found by Fürst et al. (2018) in the following sections.

8.1.1 CRSF parameter values

In the following, the CRSF parameters found in the phase-averaged spectroscopy are compared to the values found by Fürst et al. (2018) in their observation 1 (*NuSTAR* ob-

servation of 2014) for their NPEX model fit.

The line energy of CRSF1 in this thesis is generally 2 keV higher; the uncertainty intervals of Fürst’s fit and my `cutoffpl` model fits do overlap. Similarly, the parameters found here for the line energy of CRSF2 are approximately 3 keV higher than determined by Fürst et al. (2018). The uncertainty intervals of this parameter given by Fürst et al. overlaps with the intervals determined here for the NPEX and FDcut fits. The depth values of CRSF1 differ drastically from values found by Fürst et al. (2018). While I find values on the order of 11 – 12 keV, Fürst et al. find a depth of only 3.8 keV. One cannot rule out the possibility that the here found depth is a result of the CRSF model partly modeling the continuum instead of the absorption feature. In this thesis the depth of CRSF2 could only be correctly modeled with the FDcut and NPEX fits, as the `cutoffpl` model value cannot be constrained within the limits of 0 – 20 keV. Fürst et al. (2018) did permit for higher depth values, which lead to results between 20 – 27.6 keV depending on the used model.

The line energy parameters found in the phase-averaged analysis strongly indicate that the two lines are not harmonically related as their ratio is $E_{\text{CRSF2}}/E_{\text{CRSF1}} \approx 1.4 \neq 2$. It is also possible that there is a fundamental line at $E_{\text{fund.}} \approx 17$ keV, which would have harmonics at 34 keV and 51 keV. Fitting the FDcut model with three dependent CRSFs decreases the fit quality drastically; the fitted depth of the fundamental line is $d \approx 6 \cdot 10^{-12}$ keV. These are both strong indicators that this CRSF feature does not exist. A similar analysis by Fürst et al. (2018) found that a putative fundamental line at 17 keV would have a width compatible with 0 keV. For these reasons the lines are assumed to be independent, which implies that they are formed in different regions.

8.1.2 Phase-dependency of CRSF parameters

The phase-dependencies of the CRSF parameters are the most direct indicator of their forming regions. The line energies of both CRSF features show significant variations over the pulse phase of the neutron star.

For CRSF1, Fürst et al. (2018) describe their dependence as “sinusoidal” (see Fig. 9). This is not true for this observation: Fig. 23 shows that the line energy has a high-energy plateau of $E \approx 38$ keV for large parts of the pulse phase and has a dip to 32 keV between the phase 0.8 – 0.2.

The line energy of CRSF2 shows a comparably weaker pulse-phase-dependency in the *NuSTAR* observations of 2014 and 2015; considering the uncertainties of the fitted values Fürst et al. (2018) assumed a constant non-phase-dependent value of 49.6 keV for their further analysis; only one of their six bins shows a dip at an energy of $E \approx 45$ keV. In the observation at hand the line energy shows a strong pulse-phase dependency that is not consistent with a constant value with large error margins. The dependency found here can be described as sinusoidal with minimal and maximal values of approximately

46 keV and 51 keV, respectively. This phase-variability is crucial for the model of the accretion column, which is discussed in the next section.

8.2 Implications for accretion column model

To understand why the here found phase-variability of the line energy of CRSF2 has a large impact on the accretion columns of GX 301–2 the model suggested by Fürst et al. (2018) needs to be briefly introduced.

Based on a constant line energy of CRSF2 they assume that this line is formed at the neutron star surface. From this they estimate the line energy of CRSF1 as a function of altitude above the neutron star surface. For a canonical neutron star they find a height of $h \approx 1.4$ km. The mechanism responsible for the formation of CRSF1 is in this case a gas shock. Assuming a higher mass of $M_{\text{NS}} = 1.8M_{\odot}$ implies that the mechanism is Coulomb-radiation dominated. For this higher mass they give a formula for the expected shock height in terms of the luminosity and magnetic field of the neutron star (see Fürst et al., 2018, eq. 3). Fürst et al. argue that the variability of CRSF1 is caused by a change in viewing angle; this leads to Doppler boosting of the source photons towards and away from the observer depending on the pulse phase.

However, their proposed model appears to be inconsistent with the phase-dependency found in this thesis. In the following possible explanations of the formation of the observed CRSFs are briefly discussed.

Firstly, we want to revisit the idea of a fundamental line at 17 keV, where CRSF1 and CRSF2 would serve as harmonics. If all three lines are formed within the same accretion column it is expected that they show the same pulse-phase variability, as the viewing angle on the accretion column changes. This is not the case as the line energies of both detected lines show different phase-dependencies. For an analysis of the cyclotron lines of V 0332+53 where also implications for the accretion column are discussed see Lutovinov et al. (2015).

One could also argue that the lines are formed in different accretion columns, where the phase dependencies can differ from each other. A shared problem of both proposed theories is that the fundamental line at 17 keV is neither detected in this nor in Fürst's observation. This could theoretically be caused by photon spawning: electrons on high Landau levels de-excite via resonant scattering, where they transition from level n to $n - 1$; the scattered photon has an energy of $E_{\text{fund.}} = 17$ keV. This effect can partly compensate the absorption feature at the fundamental line energy. It is however unlikely that the absorption feature is completely balanced by this. To follow up on this theory it may be useful to analyze observations of the source with a higher spectral range to determine whether an absorption feature at $E \approx 67$ keV can be found in the spectrum; the existence of this 3rd harmonic would be a strong indicator that the here observed CRSF features are harmonics of a very weak 17 keV fundamental CRSF. Observing this third harmonic poses the problem that there are very few detectors with sufficient spec-

tral resolution at energies beyond 70 keV; furthermore the exponential cutoff dominates the spectral shape at high energies, which implies that long exposure times and ideally high-luminosity observations are preferable. For a detailed discussion of fundamental cyclotron lines see, e.g., Falkner (2018, Sect. 3.3.5).

Another possible explanation is that both lines are not harmonically related and form in different columns with asymmetric accretion rates. This implies that the line-forming regions are at different altitudes with varying magnetic field strengths if one assumes a dipole-field. Another implication of this is that the line energies are very sensitive to changes in mass accretion rate. When comparing Fürst's line energies to the value determined here, one sees that the line energies barely change although the accretion-fed luminosity is higher by a factor of ≈ 8 in this observation. Also, strong enough correlations between mass accretion rate and cyclotron line energy that could explain the two lines present in GX 301–2 are not observed in other systems (see Staubert et al., 2019, Fig. 9). It is therefore also unlikely that an asymmetric accretion stream causes different line energies, as the line energies appear to be at most weakly correlated with luminosity.

A third and last possible explanation of the observed dependencies is a complex magnetic field geometry. In this case one could have two accretion columns where independent CRSF features with different phase-variabilities are formed as the magnetic field strength can vary between the two columns.

It is evident that none of the possible theories above can alone describe the CRSF existence in this system. One possible explanation is the interplay of the processes described above; it is reasonable to assume that they can form both here observed cyclotron resonant scattering features.

References

- Ajello M., Atwood W.B., Axelsson M., et al., 2021, *Nat. Astron.* 5, 385
- Anders E., Grevesse N., 1989, *GCA* 53, 197
- Baade W., Zwicky F., 1934, *Phys. Rev.* 46, 76
- Ballhausen R., 2021, Dissertation, Friedrich-Alexander-Universität Erlangen-Nürnberg
- Becker P.A., Klochkov D., Schönherr G., et al., 2012, *A&A* 544, A123
- Becker P.A., Wolff M.T., 2007, *ApJ* 654, 435
- Becker W., Truemper J., 1997, *A&A* 326, 682
- Berger K., 2019, Bachelor's thesis, Friedrich-Alexander-Universität Erlangen-Nürnberg
- Bethe H.A., Wilson J.R., 1985, *ApJ* 295, 14
- Bondi H., Hoyle F., 1944, *MNRAS* 104, 273
- Burrows A., Vartanyan D., 2021, *Nat.* 589, 29
- Cash W., 1979, *ApJ* 228, 939
- Chadwick J., 1932, *Nat.* 129, 312
- Chandrasekhar S., 1931, *ApJ* 74, 81
- Davidson K., Ostriker J.P., 1973, *ApJ* 179, 585
- Doroshenko V., Santangelo A., Suleimanov V., et al., 2010, *A&A* 515, A10
- Evangelista Y., Feroci M., Costa E., et al., 2010, *ApJ* 708, 1663
- Falkner P., 2018, Dissertation, Friedrich-Alexander-Universität Erlangen-Nürnberg
- Frank J., King A., Raine D., 2012, *Accretion Power in Astrophysics*, Cambridge University Press
- Fürst F., Falkner S., Marcu-Cheatham D., et al., 2018, *A&A* 620, A153
- Fürst F., Suchy S., Kreykenbohm I., et al., 2011, *A&A* 535, A9
- Gaia CollaborationBrown, A. G. A. Vallenari, A. et al., 2021, *A&A* 649, A1
- Gaia CollaborationPrusti, T. de Bruijne, J. H. J. et al., 2016, *A&A* 595, A1

Giacconi R., Gursky H., Paolini F.R., Rossi B.B., 1962, *Phys. Rev. Lett.* 9, 439

Harrison F.A., Craig W.W., Christensen F.E., et al., 2013, *ApJ* 770, 103

Hewish A., Bell S.J., Pilkington J.D.H., et al., 1968, *Nat.* 217, 709

Janka H.T., Hanke F., Huedepohl L., et al., 2012, *Prog. Theor. Exp. Phys.*

Kaasra J.S., Bleeker J.A.M., 2016, *A&A* 587, A151

Kaper L., Lamers H.J.G.L.M., Ruymaekers E., et al., 1995, *A&A* 300, 446

Kaper L., van der Meer A., Najarro F., 2006, *A&A* 457, 595

Koh D.T., Bildsten L., Chakrabarty D., et al., 1997, *ApJ* 479, 933

Kreykenbohm I., Wilms J., Coburn W., et al., 2004, *A&A* 427, 975

Landau L., 1930, *Zeitschrift für Physik* 64, 629

Leahy D.A., Darbro W., Elsner R.F., et al., 1983, *ApJ* 266, 160

Lutovinov A.A., Tsygankov S.S., Suleimanov V.F., et al., 2015, *Monthly Notices of the Royal Astronomical Society* 448, 2175–2186

Madsen K.K., Harrison F.A., Markwardt C.B., et al., 2015, *ApJS* 220, 8

Meszáros P., Nagel W., 1985, *ApJ* 299, 138

Mihara T., Makishima K., Nagase F., 1995, In: *American Astronomical Society Meeting Abstracts*, Vol. 187. *American Astronomical Society Meeting Abstracts*, p. 104.03

Müller S., 2013, *Dissertation*, Friedrich-Alexander-Universität Erlangen-Nürnberg

Nagase F., 1989, *PASJ* 41, 1

Nakamura D., Ikeda A., Sawabe H., et al., 2018, *AIP Publishing*

Nielsen M.B., Gizon L., Schunker H., Karoff C., 2013, *A&A* 557, L10

Oppenheimer J.R., Volkoff G.M., 1939, *Phys. Rev.* 55, 374

Peng Q.h., Tong H., 2007, *MNRAS* 378, 159

Poutanen J., Mushtukov A.A., Suleimanov V.F., et al., 2013, *ApJ* 777, 115

Roberts O.J., Veres P., Baring M.G., et al., 2021, *Nat.* 589, 207

- Schmahl E., 2005, The Cash Statistic and Forward Fitting
- Schwarm F.W.M., 2017, Dissertation, Friedrich-Alexander-Universität Erlangen-Nürnberg
- Shakura N.I., Postnov K.A., Kochetkova A.Y., et al., 2015, Astronomy Reports 59, 645
- Sokolova-Lapa E., Gornostaev M., Wilms J., et al., 2021, A&A 651, A12
- Staubert R., Trümper J., Kendziorra E., et al., 2019, A&A 622, A61
- Suchy S., Fürst F., Pottschmidt K., et al., 2012, ApJ 745, 124
- Sukhbold T., Ertl T., Woosley S.E., et al., 2016, ApJ 821, 38
- Takahashi T., Abe K., Endo M., et al., 2007, PASJ 59, S35
- Tanaka Y., 1986, Observations of compact x-ray sources. In: Radiation Hydrodynamics in Stars and Compact Objects, Vol. 255. Mihalas, Dimitri and Winkler, Karl-Heinz A., p. 198
- Truemper J., Pietsch W., Reppin C., et al., 1978, ApJ Lett. 219, L105
- van Kerkwijk M.H., Kaplan D.L., 2007, Ap&SS 308, 191
- Verner D.A., Ferland G.J., Korista K.T., Yakovlev D.G., 1996, ApJ 465, 487
- Watanabe S., Sako M., Ishida M., et al., 2003, ApJ 597, L37
- Wilms J., Allen A., McCray R., 2000, ApJ 542, 914
- Özel F., Freire P., 2016, ARA&A 54, 401

9 Appendix

Listed here are the parameters of the most important fits. Their uncertainties are given as 90% confidence intervals.

The parameter `detconst FPMB` represents the factor between the measured fluxes of the detectors FPMB and FPMA. The partial covering fraction is used in accordance with equation 23, parameter k . The blackbody model is only included in the `cutoffpl` and `FDcut` fits since the soft emission in the NPEX is modelled by the positive powerlaw. The continuum and cyclotron line parameters are given as explained in section 5.1 and following. The L_{37} parameter is derived from the norm of the continuum parameters and represents the luminosity of the source in units of 10^{37}ergs^{-1} in the energy band 3 – 50keV assuming a distance of $d = 3 \text{kpc}$. The `NPEX norm 2` parameter represents the norm relative to `NPEX norm 1`, which is frozen to 1. The width of the $\text{FeK}\alpha$ and $\text{FeK}\beta$ lines are both frozen to 10^{-6}keV due to the fact that they cannot be determined with *NuSTAR*'s spectral resolution.

The line energy of the $\text{FeK}\alpha$ line is frozen to a value of 6.4keV, the line energy of the $\text{FeK}\beta$ line is set to $\text{FeK}\alpha + 0.656 \text{keV}$. The shift between the line energies stems from atomic physics and can be found in the X-ray data booklet ¹¹.

The width of the third (empirical) Gaussian feature is fixed to 0.5keV, whilst its energy and area are free parameters.

9.1 Phase-averaged spectral fits

Parameter	cutoffpl model	FDcut model	NPEX model
<code>detconst FPMB</code>	1.0368 ± 0.0012	1.0369 ± 0.0012	$1.0369^{+0.0012}_{-0.0013}$
partial covering fraction	$0.494^{+0.007}_{-0.026}$	$0.569^{+0.006}_{-0.009}$	$0.519^{+0.010}_{-0.015}$
$N_{H1} [10^{22} \text{cm}^{-2}]$	24.4 ± 0.5	$26.0^{+0.6}_{-0.4}$	$25.1^{+0.4}_{-0.6}$
$N_{H2} [10^{22} \text{cm}^{-2}]$	$(3.02^{+0.09}_{-0.07}) \times 10^2$	$(2.56^{+0.12}_{-0.08}) \times 10^2$	$(3.09 \pm 0.11) \times 10^2$
BB Norm	$0.0280^{+0.0026}_{-0.0020}$	$0.066^{+0.021}_{-0.014}$	-
BB Temperature [keV]	$0.684^{+0.018}_{-0.014}$	$0.452^{+0.025}_{-0.006}$	-
<code>cutoffpl</code> photon index	-1.10 ± 0.06	-	-
<code>cutoffpl</code> folding energy [keV]	$5.92^{+0.11}_{-0.16}$	-	-
powerlaw photon index	-	$0.23^{+0.06}_{-0.08}$	-
<code>FDcut</code> cutoff energy [keV]	-	$16.3^{+1.3}_{-1.0}$	-

¹¹https://xdb.lbl.gov/Section1/Table_1-2.pdf

FDcut folding energy [keV]	-	$6.71^{+0.34}_{-0.08}$	
NPEX photon index 1	-	-	$3.06^{+0.1}_{-0.1}$
NPEX norm 2	-	-	$(1.75^{+0.33}_{-0.20}) \times 10^{-}$
NPEX photon index 2	-	-	$-1.33^{+0.0}_{-0.0}$
NPEX folding energy [keV]	-	-	$5.56^{+0.1}_{-0.1}$
CRSF ₁ line energy [keV]	$37.3^{+1.1}_{-1.0}$	$38.6^{+1.0}_{-0.9}$	$38.0^{+1.1}_{-1.0}$
CRSF ₁ width [keV]	$7.7^{+0.7}_{-0.6}$	$8.8^{+0.9}_{-0.8}$	$8.0^{+0.9}_{-0.8}$
CRSF ₁ depth [keV]	$11.3^{+2.6}_{-2.2}$	$12.3^{+3.4}_{-2.1}$	$11.7^{+3.3}_{-2.1}$
CRSF ₂ line energy [keV]	$53.7^{+0.7}_{-0.8}$	53.4 ± 0.9	$53.1^{+1.1}_{-1.0}$
CRSF ₂ width [keV]	$7.4^{+0.4}_{-0.4}$	$5.9^{+1.1}_{-0.9}$	$6.4^{+0.9}_{-0.8}$
CRSF ₂ depth [keV]	20^{+0}_{-4}	12^{+6}_{-4}	$14.4^{+2.2}_{-1.1}$
$E_{K\alpha}$ [keV]	6.4	6.4	6.
$EW_{K\alpha}$ [photons/s/cm ²]	$(8.89 \pm 0.11) \times 10^{-3}$	$(9.00 \pm 0.11) \times 10^{-3}$	$(8.89^{+0.12}_{-0.10}) \times 10^{-}$
$E_{K\beta}$ [keV]	$E_{K\alpha} + 0.656 \text{ keV}$	$E_{K\alpha} + 0.656 \text{ keV}$	$E_{K\alpha} + 0.656 \text{ keV}$
$EW_{K\beta}$ [photons/s/cm ²]	$(1.37 \pm 0.08) \times 10^{-3}$	$(1.28 \pm 0.08) \times 10^{-3}$	$(1.34^{+0.09}_{-0.07}) \times 10^{-}$
Gauss 3 line energy [keV]	6.340 ± 0.014	6.337 ± 0.016	$6.351^{+0.01}_{-0.01}$
Gauss 3 width [keV]	0.5	0.5	0.
Gauss 3 area [photons/s/cm ²]	$(8.72 \pm 0.22) \times 10^{-3}$	$(7.26^{+0.32}_{-0.27}) \times 10^{-3}$	$(8.39^{+0.19}_{-0.26}) \times 10^{-}$
Gainshift (1) intercept [keV]	-0.0718 ± 0.0019	-0.0726 ± 0.0019	$-0.0722^{+0.002}_{-0.001}$
Gainshift (2) intercept [keV]	-0.0994 ± 0.0019	-0.1004 ± 0.0019	$-0.0999^{+0.002}_{-0.000}$
L_{37} [$10^{37} \text{ erg s}^{-1}$]	$1.90^{+0.07}_{-0.04}$	$1.79^{+0.04}_{-0.03}$	$1.96^{+0.0}_{-0.0}$
$C_{\text{stat}}/d.o.f$	966 / 538	935 / 537	937 / 53
C_{red}	1.80	1.75	1.7

Table 6: Parameters of the fits shown in section 6

Acknowledgments

Jörn Wilms for giving me the great opportunity to work at the Dr. Karl Remeis-Observatory and his very helpful comments on my work.

Ralf Ballhausen for his assistance on many physical and programming endeavors and his patience with me during online meetings.

Katrin Berger, Ekaterina Sokolova-Lapa, Jakob Stierhof and **Philipp Thalhammer** for their help and advice during the research for and writing of this thesis.

My family for their continued support.

Saskia Vollhardt for her valued backing during this time.

This research has made use of a collection of ISIS functions (ISISscripts) provided by ECAP/Remeis observatory and MIT ¹². Furthermore, the research conducted for this thesis has made use of data and software provided by the High Energy Astrophysics Science Archive Research Center (HEASARC), which is a service of the Astrophysics Science Division at NASA/GSFC.

This work has made use of data from the European Space Agency (ESA) mission *Gaia* ¹³, processed by the *Gaia* Data Processing and Analysis Consortium (DPAC) ¹⁴. Funding for the DPAC has been provided by national institutions, in particular the institutions participating in the *Gaia* Multilateral Agreement.

¹²<http://www.sternwarte.uni-erlangen.de/isis/>

¹³<https://www.cosmos.esa.int/gaia>

¹⁴<https://www.cosmos.esa.int/web/gaia/dpac/consortium>

Declaration of Authorship

I hereby certify that the thesis I am submitting is entirely my own original work except where otherwise indicated. Any use of the works of other authors is properly acknowledged at their point of use.

Date, Location

Name